NIST Special Publication 260-159

Relative Permittivity and Loss Tangent Measurement Using the NIST 60 mm Cylindrical Cavity

Michael D. Janezic
Jolene D. Splett
Kevin J. Coakley
Raian F. Kaiser
John H. Grosvenor

NIST National Institute of Standards and Technology • Technology Administration • U.S. Department of Commerce

The National Institute of Standards and Technology was established in 1988 by Congress to "assist industry in the development of technology ... needed to improve product quality, to modernize manufacturing processes, to ensure product reliability ... and to facilitate rapid commercialization ... of products based on new scientific discoveries."

NIST, originally founded as the National Bureau of Standards in 1901, works to strengthen U.S. industry's competitiveness; advance science and engineering; and improve public health, safety, and the environment. One of the agency's basic functions is to develop, maintain, and retain custody of the national standards of measurement, and provide the means and methods for comparing standards used in science, engineering, manufacturing, commerce, industry, and education with the standards adopted or recognized by the Federal Government.

As an agency of the U.S. Commerce Department's Technology Administration, NIST conducts basic and applied research in the physical sciences and engineering, and develops measurement techniques, test methods, standards, and related services. The Institute does generic and precompetitive work on new and advanced technologies. NIST's research facilities are located at Gaithersburg, MD 20899, and at Boulder, CO 80303. Major technical operating units and their principal activities are listed below. For more information visit the NIST Website at http://www.nist.gov, or contact the Publications and Program Inquiries Desk, 301-975-3058.

Office of the Director
- National Quality Program
- International and Academic Affairs

Technology Services
- Standards Services
- Technology Partnerships
- Measurement Services
- Information Services
- Weights and Measures

Advanced Technology Program
- Economic Assessment
- Information Technology and Applications
- Chemistry and Life Sciences
- Electronics and Photonics Technology

Manufacturing Extension Partnership Program
- Regional Programs
- National Programs
- Program Development

Electronics and Electrical Engineering Laboratory
- Microelectronics
- Law Enforcement Standards
- Electricity
- Semiconductor Electronics
- Radio-Frequency Technology[1]
- Electromagnetic Technology[1]
- Optoelectronics[1]
- Magnetic Technology[1]

Materials Science and Engineering Laboratory
- Intelligent Processing of Materials
- Ceramics
- Materials Reliability[1]
- Polymers
- Metallurgy
- NIST Center for Neutron Research

Chemical Science and Technology Laboratory
- Biotechnology
- Process Measurements
- Surface and Microanalysis Science
- Physical and Chemical Properties[2]
- Analytical Chemistry

Physics Laboratory
- Electron and Optical Physics
- Atomic Physics
- Optical Technology
- Ionizing Radiation
- Time and Frequency[1]
- Quantum Physics[1]

Manufacturing Engineering Laboratory
- Precision Engineering
- Manufacturing Metrology
- Intelligent Systems
- Fabrication Technology
- Manufacturing Systems Integration

Building and Fire Research Laboratory
- Applied Economics
- Materials and Construction Research
- Building Environment
- Fire Research

Information Technology Laboratory
- Mathematical and Computational Sciences[2]
- Advanced Network Technologies
- Computer Security
- Information Access
- Convergent Information Systems
- Information Services and Computing
- Software Diagnostics and Conformance Testing
- Statistical Engineering

[1] At Boulder, CO 80305
[2] Some elements at Boulder, CO

NIST Special Publication 260-159

Relative Permittivity and Loss Tangent Measurement Using the NIST 60 mm Cylindrical Cavity

Michael D. Janezic
Raian F. Kaiser
John H. Grosvenor
Electromagnetics Division
Electromagnetics and Electrical Engineering Laboratory

Jolene D. Splett
Kevin J. Coakley
Statistical Engineering Division
Information Technology Laboratory

National Institute of Standards and Technology
Boulder, Colorado 80305

September 2005

National Institute of Standards and Technology Special Publication 260-159
Natl. Inst. Stand. Technol. Spec. Publ. 260-159, 65 pages (September 2005)
CODEN: NSPUE2

U.S. GOVERNMENT PRINTING OFFICE
WASHINGTON: 2004

For sale by the Superintendent of Documents, U.S. Government Printing Office
Internet: bookstore.gpo.gov — Phone: (202) 512-1800 — Fax: (202) 512-2250
Mail: Stop SSOP, Washington, DC 20402-0001

Contents

Relative Permittivity and Loss Tangent Measurement using the NIST 60 mm Cylindrical Cavity

Michael D. Janezic[†], Jolene D. Splett[‡], Kevin J. Coakley[‡], Raian F. Kaiser[†], and John H. Grosvenor[†]

[†]Electromagnetics Division
Electronics and Electrical Engineering Laboratory
National Institute of Standards and Technology
Boulder, CO 80305 USA

[‡]Statistical Engineering Division
Information Technology Laboratory
National Institute of Standards and Technology
Boulder, CO 80305 USA

In order to develop a dielectric Standard Reference Material (SRM), a measurement system for measuring the relative permittivity and loss tangent of dielectric materials is presented. To achieve the necessary level of measurement accuracy, we selected the circular-cylindrical cavity method. Expressions for determining the relative permittivity and loss tangent are derived from theoretical models of an empty and sample-loaded circular-cylindrical cavity. We describe the circular-cylindrical cavity's specifications and the detailed measurement procedure we employed. We present a comprehensive uncertainty analysis for both the relative permittivity and loss tangent as well as a measurement assurance plan for ensuring the integrity of the measurement system.

Key words: circular-cylindrical cavity; dielectric constant; loss tangent; relative permittivity; resonator.

1. Introduction

For over fifty years, researchers have measured the relative permittivity, ϵ_r', and loss tangent, $\tan\delta$, of low-loss dielectric solids at microwave frequencies with circular-cylindrical cavities [1–4]. The circular-cylindrical cavity method remains popular today because the measurement accuracy is high over a wide range of relative permittivities and loss tangents, the cavity is simple to construct, and the dielectric samples are easily machined. In addition, the measurement theory used to calculate the sample's permittivity and loss tangent is derived from a relatively simple boundary-value problem. Because of these advantages, the NIST Electromagnetic Properties of Materials program chose this method to certify the relative permittivity and loss tangent of low-loss dielectric materials for distribution as Standard Reference Materials (SRMs).

In this paper we outline the steps taken to characterize the dielectric properties of a low-loss dielectric material. In particular, using the circular-cylindrical cavity method, we characterize the permittivity and loss tangent of cross-linked polystyrene samples at 10 GHz. We begin by describing the cylindrical cavity fixture, including details about its construction, in the Cylindrical Cavity Specifications section.

We outline the necessary measurement theory in the Cylindrical Cavity Theory section. We first derive the electromagnetic fields for a cylindrical waveguide and then extend this theory to the cases of the empty and sample-loaded cylindrical cavity. Solving the boundary-value problems for these two cases, we find expressions for the resonant frequency and quality factor of the cylindrical cavity with and without sample present, plus equations for calculating the dielectric sample's relative permittivity and loss tangent.

The Sample Specifications section discusses the criteria used for selecting cross-linked polystyrene as the first SRM material and includes details regarding the specific specimen sheet we ordered. In order to reduce the overall measurement uncertainty, we also provide guidance for selecting the sample diameter and thickness. Finally, we outline the cleaning procedure used for the samples.

In the Measurement System Characterization section, we specify how we determined the variables necessary to determine the sample's permittivity and loss tangent. The variables include sample thickness, environmental variables used to calculate the speed of light in the laboratory, length and radius of the cylindrical cavity, resonant frequency and quality factor, and the conductive metal losses of the cylindrical-cavity endplates and wall.

The Permittivity and Loss Tangent Measurements section outlines the step-by-step measurement procedure used to calculate the sample's permittivity and loss tangent. We present measurement results at 10 GHz for the 18 cross-linked polystyrene samples we considered. In order to check the consistency of the cylindrical-cavity measurements, we provide permittivity and loss tangent results for cross-linked polystyrene made with four other measurement methods. Finally, we provide additional permittivity and loss tangent data from 8 to 11 GHz to show how the dielectric properties of cross-linked polystyrene vary at frequencies near 10

GHz.

The Uncertainty Analysis section addresses how we estimated the uncertainty of both relative permittivity and loss tangent measurements. We list the possible random and systematic measurement errors and describe the Monte Carlo model we used to simulate the effects of these errors on the sample's relative permittivity and loss tangent. In order to quantify the stability of the measurement process, we outline our long-term repeatability study of cross-linked polystyrene as well as a similar study involving a single-crystal quartz check standard.

Finally, the Measurement Quality Assurance section summarizes the procedures we will employ to ensure the integrity of future cylindrical-cavity measurements. Specifically, these include the development of measurement control charts for two of the cross-linked polystyrene samples. Measurements of these two samples prior to every measurement will enable us to detect problems related to the cylindrical-cavity measurement procedure or measurement software.

2. Cylindrical Cavity Specifications

The cylindrical cavity resonator shown in Figure 1 is nominally 450 mm long and 60 mm in diameter. The cavity is primarily composed of a helically wound cylindrical waveguide terminated by two gold-plated, metallic endplates. As in References [2] and [3], we employ helical waveguide to attenuate some of the undesired resonant modes while leaving the TE_{01n} resonant modes unperturbed. Our particular helical waveguide consists of two copper wires embedded in epoxy and surrounded by a fiberglass cylinder epoxied into a steel pipe. Although we must take into account the increased surface resistance of the cylindrical waveguide walls due to the epoxy's dielectric losses in order to accurately measure the loss tangent, the benefit of eliminating many of the unwanted resonant modes outweighs this small inconvenience. A layer of heat shrink was added to the steel pipe to seal it from the water jacket.

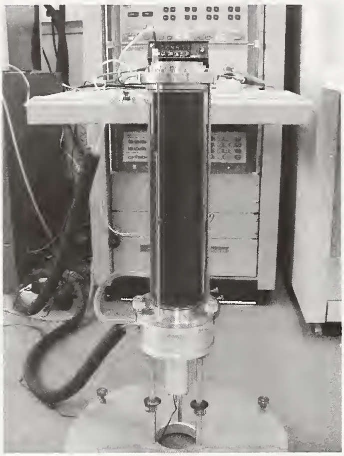

Figure 1. NIST 60 mm cylindrical cavity resonator.

The two gold-plated endplates that terminate the cylindrical cavity are optically polished. One endplate is supported by an upper flange, shown in Figure 2. The bottom endplate, with a diameter slightly smaller than that of the cylindrical waveguide, is supported by the tuning endplate assembly shown in Figure 3. Using a precision dc motor connected to a micrometer positioned below the endplate, the cylindrical cavity length can be varied by approximately one inch. The bottom endplate is connected to a yoke contained within the tuner assembly. As the motor drive moves the bottom endplate up and down within the cylindrical cavity, an electronic probe measures the change in the bottom endplate's position.

Figure 2. Upper flange of cylindrical cavity.

Figure 3. Tuning endplate assembly of cylindrical cavity.

To allow placement of a dielectric sample in the cylindrical cavity, the tuning endplate assembly is lowered so that the bottom endplate is positioned below the cylindrical waveguide section, as shown in Figure 4. The sample is then placed on the bottom endplate and the tuner assembly is raised back into position so that both the sample and bottom endplate are positioned inside the cylindrical waveguide section. In order to ensure that the bottom endplate remains parallel to the top endplate, the tuner assembly travels on three hardened-steel guide shafts.

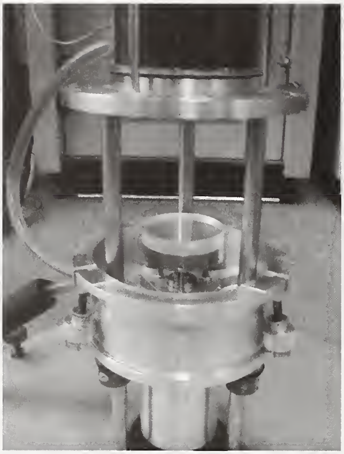

Figure 4. Dielectric sample on bottom endplate of opened, lower tuner assembly.

Located near the upper flange are two coupling loops that extend into the cavity from two circular holes located on opposite sides near the top of the cylindrical cavity. In order to excite a resonance in the cylindrical cavity, each coupling loop is connected to an automatic network analyzer via a coaxial transmission line. The extent to which the coupling loops protrude inside the cylindrical cavity is varied in order to change the degree of cavity coupling and the amplitude of the resonance. This is an improvement upon the design reported in Reference [4], where the cavity was excited by rectangular irises fed by X-band waveguide feeds. In that design, the coupling level was approximately -30 dB, resulting in significant coupling losses. With the new design, we are able to lower the coupling level to a point where the coupling losses can be neglected.

The dimensions of the cylindrical cavity must be well characterized in order to achieve high-accuracy measurements of permittivity and loss tangent. To ensure the stability of the cavity dimensions despite temperature variations in the laboratory, the cylindrical cavity is surrounded by a water jacket connected to a water bath that controls its temperature to within $\pm 0.1\,^{\circ}$C.

3. Circular-Cylindrical Cavity Theory

Before outlining the procedure for calculating the sample's relative permittivity and loss tangent, we examine the theory of an empty and a sample-loaded circular-cylindrical cavity. Specifically, we first derive the electric and magnetic fields of TE_{mn} modes in a circular-cylindrical waveguide. We then extend this theory to the resonant frequency and quality factor of the TE_{01p} mode for an empty circular-cylindrical cavity. These expressions are important for calculating the length and diameter of the cavity, as well as measuring the surface resistance of the cavity walls. Next, we consider the case of a sample-loaded cylindrical cavity and derive equations for resonant frequency and quality factor of the TE_{01p} mode used to solve for the sample's relative permittivity and loss tangent in Section 6.

3.1 Circular-Cylindrical Waveguide

For a forward-traveling wave in a circular-cylindrical waveguide the magnetic and electric fields take the form

$$\vec{H}(\rho,\phi,z) = \left[\vec{h}_T(\rho,\phi) + \vec{h}_z(\rho,\phi)\right]\exp(-\gamma z) \tag{1}$$

and

$$\vec{E}(\rho,\phi,z) = \left[\vec{e}_T(\rho,\phi) + \vec{e}_z(\rho,\phi)\right]\exp(-\gamma z), \tag{2}$$

where $\vec{h}_T$ and $\vec{e}_T$ are the transverse magnetic and electric field components, $\vec{h}_z$ and $\vec{e}_z$ are the longitudinal magnetic and electric field components, $\gamma = \alpha + j\beta$ is the propagation constant, α is the attenuation constant, and β is the phase constant. For a lossless waveguide, eqs. (1) and (2) reduce to

$$\vec{H}(\rho,\phi,z) = \left[\vec{h}_T(\rho,\phi) + \vec{h}_z(\rho,\phi)\right]\exp(-j\beta z) \tag{3}$$

and

$$\vec{E}(\rho,\phi,z) = \left[\vec{e}_T(\rho,\phi) + \vec{e}_z(\rho,\phi)\right]\exp(-j\beta z). \tag{4}$$

Since the longitudinal electric field component e_z is zero for TE_{mn} modes, we can determine the transverse electric and magnetic field components from the longitudinal magnetic field h_z.

Longitudinal Magnetic Field Component h_z

If we assume that the electromagnetic fields have $\exp(j\omega t)$ time dependence, then the wave equation for a TE_{mn} mode is

$$[\nabla^2 + \omega^2\mu_0\epsilon_0\epsilon_a' - \beta^2]h_z(\rho,\phi) = 0, \tag{5}$$

where ω is the frequency in radians, μ_0 is the permeability of free space, ϵ_0 is the permittivity of free space, and ϵ_a' is the relative permittivity of the air inside the waveguide. Expressed

in circular-cylindrical coordinates, eq. (5) becomes

$$\left[\frac{1}{\rho}\frac{\partial}{\partial\rho}\left(\rho\frac{\partial}{\partial\rho}\right)+\frac{1}{\rho^2}\frac{\partial^2}{\partial\phi^2}+k_c^2\right]h_z(\rho,\phi)=0, \tag{6}$$

where

$$k_c^2=\omega^2\mu_0\epsilon_0\epsilon_a^{'}-\beta^2. \tag{7}$$

Solutions for h_z are found using the method of separations of variables. We let

$$h_z(\rho,\phi)=R(\rho)\Phi(\phi) \tag{8}$$

and substitute this into eq. (6) to obtain

$$\frac{1}{R}\rho\frac{\partial}{\partial\rho}\left(\rho\frac{\partial R}{\partial\rho}\right)+\rho^2k_c^2=-\frac{1}{\Phi}\frac{\partial^2\Phi}{\partial\phi^2}. \tag{9}$$

Since ρ and z are independent variables, both sides of eq. (9) must equal an arbitrary constant:

$$\frac{1}{R}\rho\frac{\partial}{\partial\rho}\left(\rho\frac{\partial R}{\partial\rho}\right)+\rho^2k_c^2=-\frac{1}{\Phi}\frac{\partial^2\Phi}{\partial\phi^2}=k_\phi^2, \tag{10}$$

where k_ϕ^2 is the separation constant.

Solution for $\Phi(\phi)$

The solution to the differential equation

$$\frac{d^2\Phi}{d\phi^2}+k_\phi^2\Phi=0 \tag{11}$$

is

$$\Phi(\phi)=A_0\cos(k_\phi\phi)+B_0\sin(k_\phi\phi), \tag{12}$$

where A_0 and B_0 are constants. Since the fields must be periodic in ϕ, we can apply two boundary conditions. First, enforcing

$$\Phi(\pi)=\Phi(-\pi), \tag{13}$$

we find

$$B_0=0. \tag{14}$$

With the second boundary condition

$$\frac{d\Phi}{d\phi}|_{\phi=\pi}=\frac{d\Phi}{d\phi}|_{\phi=-\pi}, \tag{15}$$

we find

$$k_\phi=m, \qquad \text{where } m=1,2,3,\ldots \quad . \tag{16}$$

Thus, the solution to eq. (11) is

$$\Phi(\phi)=A_0\cos(m\phi). \tag{17}$$

Solution for $R(\rho)$

The solution to the differential equation

$$\frac{1}{R}\rho\frac{d}{d\rho}\left(\rho\frac{dR}{d\rho}\right) + \rho^2 k_c^2 = k_\phi^2 \tag{18}$$

is

$$R(\rho) = A_1 J_m(k_c\rho) + B_1 Y_m(k_c\rho), \tag{19}$$

where A_1 and B_1 are constants, J_m is the Bessel function of the first kind of order m, and Y_m is the Bessel function of the second kind of order m. The fields must be finite inside the circular waveguide, so from the condition that

$$|R(\rho \to 0)| \text{ is finite,} \tag{20}$$

we find

$$B_1 = 0. \tag{21}$$

We also assume that the metallic walls of the circular waveguide are made up of perfect conductors, so that

$$\frac{d}{d\rho}\left[R(\rho)\right]|_{\rho=a} = 0, \tag{22}$$

which yields

$$k_c = \frac{j'_{mn}}{a}, \tag{23}$$

where a is the radius of the waveguide and j'_{mn} is the nth zero of $J'_m(k_c\rho)$. The solution to eq. (19) is therefore

$$R(\rho) = A_1 J_m(k_c\rho). \tag{24}$$

Substituting eqs. (17) and (24) into eq. (8) we have

$$h_z(\rho,\phi) = A J_m(k_c\rho)\cos(m\phi). \tag{25}$$

Transverse Electric and Magnetic Field Components

With the expression for h_z in eq. (25), we solve for the tranverse electric field components using

$$(\omega^2\mu_0\epsilon_0\epsilon'_a - \beta^2)\vec{e}_T(\rho,\phi) = j\omega\mu_0\vec{a}_z \times \nabla h_z(\rho,\phi). \tag{26}$$

Substituting eq. (25) into eq. (26) we get

$$e_\rho(\rho,\phi) = A\frac{j\omega\mu_0}{k_c^2}\frac{m}{\rho}\sin(m\phi)J_m(k_c\rho), \tag{27}$$

$$e_\phi(\rho,\phi) = A\frac{j\omega\mu_0}{k_c^2}\cos(m\phi)\left[\frac{m}{\rho}J_m(k_c\rho) - k_c J_{m+1}(k_c\rho)\right]. \tag{28}$$

In the same way, we find the transverse magnetic field components using

$$(\omega^2\mu_0\epsilon_0\epsilon_a^{'} - \beta^2)\vec{h}_T(\rho,\phi) = -j\beta\,\nabla h_z(\rho,\phi). \tag{29}$$

Substituting eq. (25) into eq. (29) we get

$$h_\rho(\rho,\phi) = -A\frac{j\beta}{k_c^2}\cos(m\phi)\left[\frac{m}{\rho}J_m(k_c\rho) - k_cJ_{m+1}(k_c\rho)\right], \tag{30}$$

$$h_\phi(\rho,\phi) = A\frac{j\beta}{k_c^2}\frac{m}{\rho}\sin(m\phi)J_m(k_c\rho). \tag{31}$$

Electric and Magnetic Fields

Knowing the electric and magnetic field components, we can write expressions for the magnetic and electric fields of a TE_{mn} mode in a circular-cylindrical waveguide:

$$E_\rho(\rho,\phi,z) = A\frac{j\omega\mu_0}{k_c^2}\frac{m}{\rho}\sin(m\phi)J_m(k_c\rho)\exp(-j\beta z), \tag{32}$$

$$E_\phi(\rho,\phi,z) = A\frac{j\omega\mu_0}{k_c^2}\cos(m\phi)\left[\frac{m}{\rho}J_m(k_c\rho) - k_cJ_{m+1}(k_c\rho)\right]\exp(-j\beta z), \tag{33}$$

$$E_z(\rho,\phi,z), = 0 \tag{34}$$

$$H_\rho(\rho,\phi,z) = -A\frac{j\beta}{k_c^2}\cos(m\phi)\left[\frac{m}{\rho}J_m(k_c\rho) - k_cJ_{m+1}(k_c\rho)\right]\exp(-j\beta z), \tag{35}$$

$$H_\phi(\rho,\phi,z) = A\frac{j\beta}{k_c^2}\frac{m}{\rho}\sin(m\phi)J_m(k_c\rho)\exp(-j\beta z), \tag{36}$$

$$H_z(\rho,\phi,z) = AJ_m(k_c\rho)\cos(m\phi)\exp(-j\beta z), \tag{37}$$

where

$$k_c^2 = \omega^2\mu_0\epsilon_0\epsilon_a^{'} - \beta^2, \tag{38}$$

$$k_c = \frac{j_{mn}^{'}}{a}. \tag{39}$$

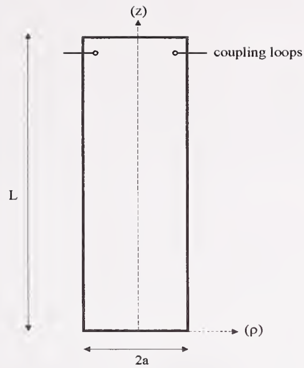

Figure 5. Empty cylindrical cavity.

3.2 Empty Circular-Cylindrical Cavity

3.2.1 Electric and Magnetic Fields

In a circular-cylindrical cavity, shown in Figure 5, the two ends of a circular waveguide are terminated with conductive plates. The boundary conditions along the waveguide walls are the same as those of the circular waveguide, and the radial and circumferential variations in the electric and magnetic fields remain the same. However, since there are standing waves in the cavity instead of a traveling wave propagating along the axis of the circular waveguide, we must modify the z-dependence of the electric and magnetic fields. If we assume a standing wave inside the cavity, the electric field components are

$$E_\rho(\rho,\phi,z) = A\frac{j\omega\mu_0}{k_c^2}\frac{m}{\rho}\sin(m\phi)J_m(k_c\rho)\left[B\sin(\beta z)+C\cos(\beta z)\right], \tag{40}$$

$$E_\phi(\rho,\phi,z) = A\frac{j\omega\mu_0}{k_c^2}\cos(m\phi)\left[\frac{m}{\rho}J_m(k_c\rho)-k_cJ_{m+1}(k_c\rho)\right]\left[B\sin(\beta z)+C\cos(\beta z)\right], \tag{41}$$

where B and C are constants to be determined. Assuming that the two endplates are perfectly conducting, the tangential electric fields at $z=0$ and $z=L$ are zero. Applying these two boundary conditions on E_ρ and E_ϕ, we find that

$$C = 0, \tag{42}$$

and

$$\beta = \frac{p\pi}{L}, \quad p = 1,2,3,\dots \tag{43}$$

Therefore, eqs. (40) and (41) reduce to

$$E_\rho(\rho,\phi,z) = A\frac{j\omega\mu_0}{k_c^2}\frac{m}{\rho}\sin(m\phi)J_m(k_c\rho)\sin(\beta z), \tag{44}$$

$$E_\phi(\rho,\phi,z) = A\frac{j\omega\mu_0}{k_c^2}\cos(m\phi)\left[\frac{m}{\rho}J_m(k_c\rho) - k_cJ_{m+1}(k_c\rho)\right]\sin(\beta z). \tag{45}$$

Using Faraday's law,

$$\nabla \times \vec{E} = -j\omega\mu_0\vec{H}, \tag{46}$$

we can find the magnetic field components as follows:

$$H_\rho(\rho,\phi,z) = A\frac{\beta}{k_c^2}\cos(m\phi)\left[\frac{m}{\rho}J_m(k_c\rho) - k_cJ_{m+1}(k_c\rho)\right]\cos(\beta z), \tag{47}$$

$$H_\phi(\rho,\phi,z) = -A\frac{\beta}{k_c^2}\frac{m}{\rho}\sin(m\phi)J_m(k_c\rho)\cos(\beta z), \tag{48}$$

$$H_z(\rho,\phi,z) = AJ_m(k_c\rho)\cos(m\phi)\sin(\beta z). \tag{49}$$

In particular, the electric and magnetic fields for a TE_{01p} mode are

$$E_\rho(\rho,\phi,z) = 0, \tag{50}$$

$$E_\phi(\rho,\phi,z) = -A\frac{j\omega\mu_0}{k_c}J_1(k_a\rho)\sin(\beta z), \tag{51}$$

$$H_\rho(\rho,\phi,z) = -A\frac{\beta}{k_c}J_1(k_a\rho)\cos(\beta z), \tag{52}$$

$$H_\phi(\rho,\phi,z) = 0, \tag{53}$$

$$H_z(\rho,\phi,z) = AJ_0(k_c\rho)\sin(\beta z). \tag{54}$$

3.2.2 TE_{01p} Mode Resonant Frequency

For the TE_{mnp} resonant mode, the electric- and magnetic-field components are

$$E_\rho(\rho,\phi,z) = A\frac{j\omega\mu_0}{k_c^2}\frac{m}{\rho}\sin(m\phi)J_m(k_c\rho)\sin(\beta z), \tag{55}$$

$$E_\phi(\rho,\phi,z) = A\frac{j\omega\mu_0}{k_c^2}\cos(m\phi)\left[\frac{m}{\rho}J_m(k_c\rho) - k_cJ_{m+1}(k_c\rho)\right]\sin(\beta z), \tag{56}$$

$$H_\rho(\rho,\phi,z) = A\frac{\beta}{k_c^2}\cos(m\phi)\left[\frac{m}{\rho}J_m(k_c\rho) - k_cJ_{m+1}(k_c\rho)\right]\cos(\beta z), \tag{57}$$

$$H_\phi(\rho,\phi,z) = -A\frac{\beta}{k_c^2}\frac{m}{\rho}\sin(m\phi)J_m(k_c\rho)\cos(\beta z), \tag{58}$$

$$H_z(\rho,\phi,z) = AJ_m(k_c\rho)\cos(m\phi)\sin(\beta z), \tag{59}$$

where

$$k_c^2 = \omega^2\mu_0\epsilon_0\epsilon_a^{'} - \beta^2, \tag{60}$$

$$k_c = \frac{j'_{mn}}{a}, \tag{61}$$

and

$$\beta = \frac{p\pi}{L}. \tag{62}$$

Substituting eqs. (61) and (62) into eq. (60), one can determine the resonant frequency, f_{mnp}, of the TE_{mnp} mode as

$$f_{mnp} = \frac{c_{air}}{2\pi}\left[\left(\frac{j'_{mn}}{a}\right)^2 + \left(\frac{p\pi}{L}\right)^2\right]^{\frac{1}{2}}, \tag{63}$$

where

$$c_{air} = \frac{1}{\sqrt{\mu_0\epsilon_0\epsilon'_a}}. \tag{64}$$

For the case of the TE_{01p} mode, eq. (63) reduces to

$$f_{01p} = \frac{c_{air}}{2\pi}\left[\left(\frac{j'_{01}}{a}\right)^2 + \left(\frac{p\pi}{L}\right)^2\right]^{\frac{1}{2}}. \tag{65}$$

3.2.3 TE_{01p} Mode Quality Factor

One of the more important parameters of a cavity is its quality factor, Q. In particular we are interested in the quality factor of the TE_{01p} mode. The quality factor for the empty cylindrical cavity is defined as

$$Q \equiv \omega\frac{\text{stored energy in cavity}}{\text{dissipated power in cavity}} = \omega\frac{W_0}{P_w + P_b + P_t}, \tag{66}$$

where ω is the resonant frequency of the TE_{01p} mode in radians, W_0 is the time-averaged energy stored within the cavity, P_w is the power dissipated on the cavity wall, P_b is the power dissipated on the bottom cavity endplate, and P_t is the power dissipated on the top cavity endplate. If there were no conductive losses within the cavity, the denominator of eq. (66) would be zero and the quality factor would approach infinity. However, for real conductors, there is power dissipated in the cavity walls and endplates, and the quality factor is some finite value.

Using the electric and magnetic fields for the TE_{01p} mode (50-54), we derive expressions for the both the stored energy and dissipated power in the cavity:

$$W_0 = \frac{\epsilon_0\epsilon'_a}{2}\int_V |E|^2\,dv = \frac{\epsilon_0\epsilon'_a}{2}\int_{z=0}^{L}\int_{\rho=0}^{a}\int_{\phi=0}^{2\pi}|E_\phi|^2\rho\,d\rho\,d\phi\,dz = A^2\frac{\pi\epsilon_0\epsilon'_a\omega^2\mu_0^2a^2L}{4k^2}J_0^2(ka), \tag{67}$$

$$P_w = \frac{R_{sw}}{2}\oint_S |H|^2 ds = \frac{R_{sw}}{2}\int_{z=0}^{L}\int_{\phi=0}^{2\pi}|H_z|^2\rho\,d\rho\,dz\,\Big|_{\rho=a} = A^2\frac{\pi a L}{2}J_0^2(ka)R_{sw}, \tag{68}$$

$$P_b = \frac{R_{sb}}{2} \oint_S |H|^2 ds = \frac{R_{sb}}{2} \int_{\rho=0}^{a} \int_{\phi=0}^{2\pi} |H_\rho|^2 \rho \, d\phi \, dz \Big|_{z=0} = A^2 \frac{\pi \beta_a^2 a^2}{2k^2} J_0^2(ka) R_{sb}, \tag{69}$$

and

$$P_t = \frac{R_{st}}{2} \oint_S |H|^2 ds = \frac{R_{st}}{2} \int_{\rho=0}^{a} \int_{\phi=0}^{2\pi} |H_\rho|^2 \rho \, d\phi \, dz \Big|_{z=L} = A^2 \frac{\pi \beta_a^2 a^2}{2k^2} J_0^2(ka) R_{st}, \tag{70}$$

where R_{sw}, R_{sb}, and R_{st} are the surface resistivities of the cavity wall, bottom endplate, and top endplate. Substituting eqs. (67-70) into eq. (66) we obtain the expression for the quality factor of the TE_{01p} mode,

$$Q = \frac{\frac{1}{2}\sqrt{\frac{\mu_0}{\epsilon_0 \epsilon_a'}} \left[\left(\frac{j_{01}'}{a} \right)^2 + \left(\frac{p\pi}{L} \right)^2 \right]^{3/2}}{\frac{1}{L} \left(\frac{p\pi}{L} \right)^2 [R_{sb} + R_{st}] + \frac{1}{a} \left(\frac{j_{01}'}{a} \right)^2 R_{sw}}. \tag{71}$$

3.3 Sample-Loaded Circular-Cylindrical Cavity

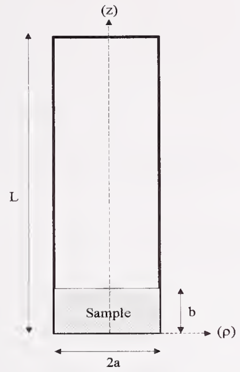

Figure 6. Sample-loaded circular-cylindrical cavity.

3.3.1 Electric and Magnetic Fields in the Air-Filled Region

For the TE_{01p} mode, only the azimuthal ϕ-component of the electric field exists:

$$E_{0\phi}(\rho, z) = -A_0 \frac{j\omega\mu_0}{k_c} J_1(k_c\rho)\left[B_0 \sin(\beta_0 z) + C_0 \cos(\beta_0 z)\right], \tag{72}$$

where

$$\beta_0^2 = \omega^2 \mu_0 \epsilon_0 \epsilon_a^{'} - k_c^2, \tag{73}$$

and $\epsilon_a^{'}$ is the relative permittivity of the air. The tangential electric field must be zero on the upper cavity endplate. Therefore, applying the boundary condition

$$E_{0\phi}(\rho, z = L) = 0, \tag{74}$$

we find that

$$C_0 = -B_0 \tan(\beta_0 L). \tag{75}$$

Therefore, the electric field in the air-filled cavity region is

$$E_{0\phi}(\rho, z) = -A_0 \frac{j\omega\mu_0}{k} J_1(k_c\rho)\left[\sin(\beta_0 z) - \tan(\beta_0 L)\cos(\beta_0 z)\right]. \tag{76}$$

Using Faraday's law,

$$\nabla \times \vec{E} = -j\omega\mu_0 \vec{H}, \tag{77}$$

we can find the remaining magnetic field components:

$$H_{0\rho}(\rho, z) = -A_0 \frac{\beta_0}{k_c} J_1(k_c \rho) \left[\cos(\beta_0 z) + \tan(\beta_0 L)\sin(\beta_0 z)\right] \quad (78)$$

$$H_{0z}(\rho, z) = A_0 J_0(k_c \rho) \left[\sin(\beta_0 z) - \tan(\beta_0 L)\cos(\beta_0 z)\right]. \quad (79)$$

3.3.2 Electric and Magnetic Fields in the Sample-Filled Region

The electric and magnetic fields in the sample-filled region are derived in a manner similar to that for the air-filled region. As in that case, only the ϕ-component of the electric field exists:

$$E_{1\phi}(\rho, z) = -A_1 \frac{j\omega\mu_0}{k_c} J_1(k_c \rho) \left[B_1 \sin(\beta_s z) + C_1 \cos(\beta_s z)\right], \quad (80)$$

where

$$\beta_s^2 = \omega^2 \mu_0 \epsilon_0 \epsilon_s^{'} - k_c^2, \quad (81)$$

and $\epsilon_s^{'}$ is the relative permittivity of the sample. The tangential electric field must be zero on the bottom cavity endplate. Therefore, applying the boundary condition

$$E_{1\phi}(\rho, z = 0) = 0, \quad (82)$$

we find that

$$C_1 = 0. \quad (83)$$

Therefore, the electric field in the sample-filled region reduces to

$$E_{1\phi}(\rho, z) = -A_1 \frac{j\omega\mu_0}{k_c} J_1(k_c \rho) \sin(\beta_s z). \quad (84)$$

Using eq. (77), we find the remaining magnetic field components:

$$H_{1\rho}(\rho, z) = -A_1 \frac{\beta_s}{k_c} J_1(k_c \rho) \cos(\beta_s z), \quad (85)$$

$$H_{1z}(\rho, z) = A_1 J_0(k_c \rho) \sin(\beta_s z). \quad (86)$$

3.3.3 TE_{01p} Mode Resonant Frequency

In order to determine the TE_{01p} resonant frequencies for the sample-loaded cavity, we must match the tangential electric and magnetic fields at the sample-air boundary $z = b$. From the boundary condition on the tangential electric field,

$$E_{0\phi}(\rho, \phi, z = b) = E_{1\phi}(\rho, \phi, z = b), \quad (87)$$

we get

$$A_1 \sin(\beta_s b) = A_0 \left[\sin(\beta_0 b) - \tan(\beta_0 L)\cos(\beta_0 b)\right]. \quad (88)$$

From the boundary condition on the tangential magnetic field,

$$H_{0\rho}(\rho, \phi, z = b) = H_{1\rho}(\rho, \phi, z = b), \tag{89}$$

we get

$$A_1 \beta_s \cos(\beta_s b) = A_0 \beta_0 \left[\cos(\beta_0 b) + \tan(\beta_0 L) \sin(\beta_0 b)\right]. \tag{90}$$

Combining eqs. (88) and (90) we get

$$\frac{\tan(\beta_s b)}{\beta_s} + \frac{\tan\left[\beta_0(L - b)\right]}{\beta_0} = 0. \tag{91}$$

In the case of the empty cavity, we can calculate the resonant frequencies by use of eq. (63). This is not the case for the sample-loaded cavity. We must use an iterative technique to find the zeroes of eq. (91). The p-th zero of this function is the resonant frequency of the TE_{01p} mode. Note that this equation can also be used to obtain the relative permittivity of the sample ϵ_s' when the resonant frequency is measured.

3.3.4 TE_{01p} Mode Quality Factor

As in the case of the air-filled cylindrical cavity, we can derive an expression for the quality factor of the sample-loaded cavity. In particular, we derive an expression for the quality factor of the TE_{01p} mode. The quality factor is defined as

$$Q \equiv \omega \frac{\text{stored energy in cavity}}{\text{dissipated power in cavity}} = \omega \frac{W_s + W_a}{P_{ws} + P_{wa} + P_b + P_t + P_s}, \tag{92}$$

where ω is the resonant frequency of the TE_{01p} mode in radians, W_s is the time-averaged energy stored within the air-filled portion of the cavity, W_a is the time-averaged energy stored within the sample-filled portion of the cavity, P_{ws} is the power dissipated on the cavity wall in the sample-filled region, P_{wa} is the power dissipated along the cavity wall in the air-filled region, P_b is the power dissipated on the bottom endplate, P_t is the power dissipated on the top endplate, and P_s is the power dissipated in the sample.

Using the electric and magnetic field for the TE_{01p} mode, we derive expressions for both the stored-energy and dissipated-power terms in the sample-loaded cylindrical cavity:

$$W_s = \frac{\epsilon_0 \epsilon_s'}{2} \int_{z=0}^{b} \int_{\rho=0}^{a} \int_{\phi=0}^{2\pi} |E_{1\phi}|^2 \rho \, d\rho \, d\phi \, dz = A_1^2 \frac{\pi \epsilon_0 \epsilon_s' \omega^2 \mu_0^2 a^2}{8k^2} J_0^2(ka) \left[2b - \frac{\sin 2\beta_s b}{\beta_s}\right], \tag{93}$$

$$W_a = \frac{\epsilon_0 \epsilon_a'}{2} \int_{z=b}^{L} \int_{\rho=0}^{a} \int_{\phi=0}^{2\pi} |E_{0\phi}|^2 \rho \, d\rho \, d\phi \, dz = A_0^2 \frac{\pi \epsilon_0 \epsilon_a' \omega^2 \mu_0^2 a^2}{8k^2 \cos^2(\beta_0 L)} J_0^2(ka) \left[2(L - b) - \frac{\sin\left[2\beta_0(L - b)\right]}{\beta_0}\right], \tag{94}$$

$$P_{ws} = \frac{R_{sw}}{2} \int\limits_{z=0}^{b} \int\limits_{\phi=0}^{2\pi} |H_{1z}|^2 \rho \, d\phi \, dz \,\Big|_{\rho=a} = A_1^2 \frac{\pi a}{4} J_0^2(ka) \left[2b - \frac{\sin 2\beta_s b}{\beta_s}\right] R_{sw}, \tag{95}$$

$$P_{wa} = \frac{R_{sw}}{2} \int\limits_{z=b}^{L} \int\limits_{\phi=0}^{2\pi} |H_{0z}|^2 \rho \, d\phi \, dz \,\Big|_{\rho=a} = A_0^2 \frac{\pi a}{4} J_0^2(ka) \frac{1}{\cos^2 \beta_0 L} \left[2(L-b) - \frac{\sin\left[2\beta_0(L-b)\right]}{\beta_0}\right] R_{sw}, \tag{96}$$

$$P_b = \frac{R_{sb}}{2} \int\limits_{\rho=0}^{a} \int\limits_{\phi=0}^{2\pi} |H_{1\rho}|^2 \rho \, d\phi \, d\rho \,\Big|_{z=0} = A_1^2 \frac{\pi \beta_s^2 a^2}{2k^2} J_0^2(ka) R_{sb}, \tag{97}$$

$$P_t = \frac{R_{st}}{2} \int\limits_{\rho=0}^{a} \int\limits_{\phi=0}^{2\pi} |H_{0\rho}|^2 \rho \, d\phi \, d\rho \,\Big|_{z=L} = A_0^2 \frac{\pi \beta_a^2 a^2}{2k^2} \frac{1}{\cos^2 \beta_0 L} J_0^2(ka) R_{st}, \tag{98}$$

$$P_s = \frac{1}{2} \tan \delta_s \omega \epsilon_0 \epsilon_s' \int\limits_{\rho=0}^{a} \int\limits_{z=0}^{b} \int\limits_{\phi=0}^{2\pi} |E_{1\phi}|^2 \rho \, d\phi \, d\rho \, dz = A_1^2 \tan \delta_s \epsilon_0 \epsilon_s' \frac{\pi \omega^3 \mu_0^2 a^2}{8k^2} J_0^2(ka) \left[2b - \frac{\sin(2\beta_s b)}{\beta_s}\right]. \tag{99}$$

Solving eq. (92) for the sample loss tangent $\tan \delta_s$, we get

$$\tan \delta_s = \left[\frac{\omega(W_a + W_s)}{Q} - P_{ws} - P_{wa} - P_b - P_t\right] \left\{A_1^2 \epsilon_0 \epsilon_s' \frac{\pi \omega^3 \mu_0^2 a^2}{8k^2} J_0^2(ka) \left[2b - \frac{\sin(2\beta_s b)}{\beta_s}\right]\right\}^{-1}. \tag{100}$$

Note that several variables must be measured or calculated before we can employ eq. (100) to calculate the loss tangent of the sample. In the case of the sample, we must know its dimensions and permittivity. For the cylindrical cavity, we must also know the cavity dimensions and the microwave surface resistivities of the cavity wall and endplates. In addition to these quantities, we must measure the resonant frequency and quality factor when the sample is present in the cylindrical cavity. As for the unknown constants A_0 and A_1, we arbitrarily set A_1 to unity and determine A_0 in term of A_1 from eq. (90).

4. Sample Specifications

4.1 SRM Sample Selection

Our criteria for selecting a Standard Reference Material (SRM) for permittivity and loss tangent measurements included linearity, homogeneity, isotropy and stability with changes in temperature and frequency [5]. Based on these criteria, we selected cross-linked polystyrene as the first low-loss, low-permittivity material to be characterized as an SRM. Specifically, we purchased a 61 cm $\times$ 61 cm $\times$ 1.9 cm sheet of Rexolite 1422[1] a thermoset cross-linked styrene copolymer.

To prepare for the machining of the SRM samples, we divided the sheet into 56 sections as shown Figure 7. The first row was reserved for making preliminary SRM samples in order to refine the machining process as well as to make samples for measuring the permittivity and loss tangent using other measurement methods. Eighteen samples, whose locations are shown in bold in Figure 7, were fabricated into cylindrical samples that fit inside the 60 mm cylindrical cavity. We discuss the SRM sample dimensions and tolerances in the following sections.

1	2	3	4	5	6	7	8
9	**10**	11	**12**	13	14	**15**	**16**
17	18	19	20	21	22	23	**24**
25	26	27	**28**	**29**	30	31	32
33	34	35	**36**	**37**	38	39	40
41	42	43	44	45	46	47	**48**
49	**50**	51	52	**53**	54	**55**	**56**

Figure 7. Subdivision of cross-linked polystyrene sheet. Bold sites indicate the location of the first 18 cavity samples.

4.2 Sample Dimensions

4.2.1 Sample Diameter

The first quantity we considered was the diameter of the sample. To allow the sample to fit within the cavity, the diameter of the sample must be slightly less than the diameter of the cylindrical cavity. Therefore, we specified the diameter of the sample to be 59.7

[1]Certain commercial equipment, instruments, or materials are identified in this paper only to provide complete technical description. Such identification does not imply recommendation or endorsement by the National Institute of Standards and Technology, nor does it imply that the materials or equipment identified are necessarily the best available for the purpose.

mm, 0.3 mm less than the nominal cavity diameter of 60 mm. The theory for determining the sample permittivity assumes an ideal sample with no airgap between the sample and cavity. However, given that the gap is small, and that the permittivity of the cross-linked polystyrene sample is low ($\approx$2.54), and that the electric field near the cavity wall approaches zero, we expect no systematic error on the permittivity due to this small air gap [6] [7].

4.2.2 Sample Thickness

The next quantity we specified was the thickness of the sample. Since the bottom cavity endplate and the faces of the dielectric sample are not perfectly flat, there exists a residual gap between the sample and the endplate. Because the size of this gap depends on the machining quality of both the sample and endplate, the gap will vary for each sample and is difficult to characterize [8]. In order to minimize the effect of this gap and the imperfections of the machining process on the sample's top and bottom surface, we specified the sample thickness to be an integer multiple of half-wavelengths in the sample, thus forcing the electric field to be nearly zero on both the top and bottom surfaces of the sample. References [3] and [4] show that the uncertainty in the sample permittivity due to uncertainty in the sample thickness is minimized when the sample thickness is an integer multiple of a half-wavelength in the sample.

For a TE_{01p} mode, the expression for a half-guided wavelength $\lambda/2$ in the sample located inside the cylindrical cavity is

$$\frac{\lambda}{2} = \frac{\pi}{\sqrt{\omega^2 \mu_0 \epsilon_0 \epsilon_s' - \left(\frac{j_{01}'}{a}\right)^2}}, \tag{101}$$

where ω is the resonant frequency in radians, μ_0 is the permeability of free space, ϵ_0 is the permittivity of free space, ϵ_s' is the relative permittivity of the sample, j_{01}' is the first zero of $J_0'(k_c\rho)$, and a is the radius of the cylindrical cavity.

For measurements of the SRM samples at 10 GHz in a cylindrical cavity with a radius of 30 mm, and a relative permittivity of 2.535 for cross-linked polystyrene, we obtained an optimal sample thickness value of approximately 10.2 mm using eq. (101).

4.3 Sample Cleaning

Prior to any measurements, contaminants on the surfaces of the samples should be removed as they can be a source of measurement error, especially for the measurement of loss tangent. These contaminants include particles and lubricants used in the fabrication process as well as oils from handling. To remove the contaminants, we cleaned each sample with 99 % pure isopropyl alcohol and a lint-free cloth. In addition, we used lint-free gloves and avoided contact with the top and bottom sample faces.

5. Measurement System Characterization

5.1 Sample Thickness Estimation

We used a Sylvac electronic probe, shown in Figure 8, to measure the sample thickness b at 21 different locations on the sample. A circular template with 21 small holes defines the (x, y) measurement locations (see Figure 9). In addition, the sample radius was measured eight times using a caliper.

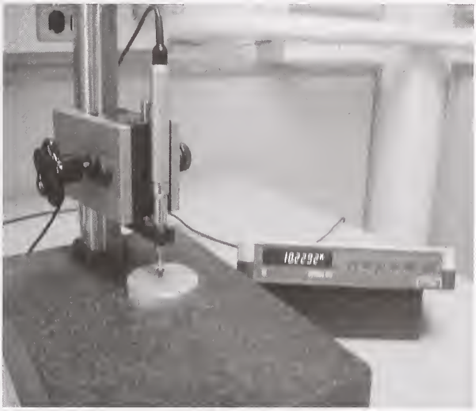

Figure 8. Electronic probe station for measuring sample thickness.

We modeled the spatially varying measured thickness of a cross-linked polystyrene sample with the polynomial model

$$b_{ij} = a_0 + a_1 \left(\frac{x_i}{R_0}\right) + a_2 \left(\frac{y_j}{R_0}\right) + a_3 \left(\frac{x_i}{R_0}\right)\left(\frac{y_j}{R_0}\right) + a_4 \left(\frac{x_i}{R_0}\right)^2 + a_5 \left(\frac{y_j}{R_0}\right)^2 + \epsilon_{ij}. \quad (102)$$

Using the method of ordinary least squares, we estimated a_0, a_1, a_2, a_3, a_4, and a_5. The (x, y) coordinates are scaled by

$$R_0 = \frac{1}{n} \sum_{i=1}^{n} R_i, \quad (103)$$

where R_i is the nth measurement of the radius of the sample. The estimated mean thickness of the sample is

$$\hat{\hat{b}} = \frac{\int \hat{b} dA}{\int dA}, \quad (104)$$

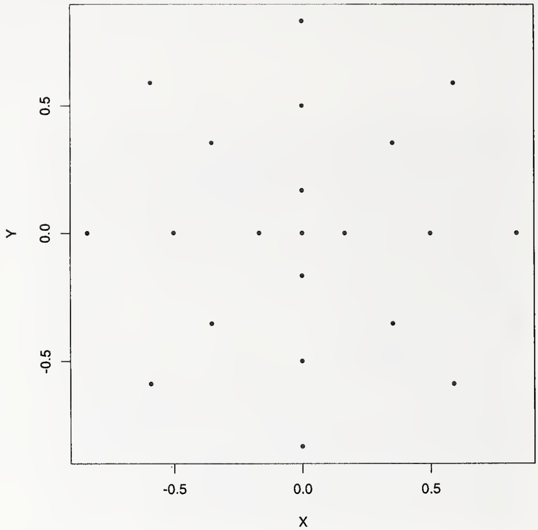

Figure 9. Thickness measurement locations.

where

$$\hat{b} = \hat{a}_0 + \hat{a}_1 \left(\frac{x_i}{R_0}\right) + \hat{a}_2 \left(\frac{y_j}{R_0}\right) + \hat{a}_3 \left(\frac{x_i}{R_0}\right)\left(\frac{y_j}{R_0}\right) + \hat{a}_4 \left(\frac{x_i}{R_0}\right)^2 + \hat{a}_5 \left(\frac{y_j}{R_0}\right)^2. \tag{105}$$

Based on eqs. (104) and (105), we estimated the mean thickness as

$$\hat{\hat{b}} = \hat{a}_0 + \frac{1}{4}\hat{a}_4 + \frac{1}{4}\hat{a}_5. \tag{106}$$

Assuming that our model is valid, we modeled the random variability of the $\hat{\hat{b}}$ measurements as

$$\mathrm{VAR}(\hat{\hat{b}}) = s_A^2 + s_B^2 + s_T^2, \tag{107}$$

where

$$
\begin{aligned}
s_A^2 &= \mathrm{VAR}(\hat{a}_0) + \frac{1}{16}[\mathrm{VAR}(\hat{a}_4) + \mathrm{VAR}(\hat{a}_5)] \\
&+ \frac{1}{2}[\mathrm{COV}(\hat{a}_0, \hat{a}_4) + \mathrm{COV}(\hat{a}_0, \hat{a}_5)] + \frac{1}{8}\mathrm{COV}(\hat{a}_4, \hat{a}_5), \qquad (108)
\end{aligned}
$$

and

$$
s_B^2 = \left(\frac{\hat{a}_4 + \hat{a}_5}{4}\right)^2 \mathrm{VAR}\left[\overline{\left(\frac{R}{R_0}\right)^2}\right]. \qquad (109)
$$

Whereas s_A^2 represents random error of the estimate (assuming that the model is valid) given perfect knowledge of the sample radius and template coordinates, the quantity s_B^2 represents uncertainty due to inexact knowledge of R. The quantity s_T^2 represents uncertainty due to inexact knowledge of template placement.

To compute s_T, we assume that all the (x, y) locations in the model have the same translation error (ϵ_x, ϵ_y). We generate new (x, y) coordinates, (x', y'), using

$$
x_i' = x_i + \epsilon_x \qquad (110)
$$

and

$$
y_i' = y_i + \epsilon_y, \qquad (111)
$$

where ϵ_x and ϵ_y are normally distributed random variables each with a mean of zero and variance σ^2, and $\sigma = pR_0$. A plausible value of p is 0.02. One hundred sets of 21 (x', y') coordinates were generated, and $\hat{\bar{b}}$ is estimated based on the polynomial model for each set of coordinates using the 21 observed thickness measurements. The standard deviation of these 100 thickness estimates is s_T.

The estimated polynomial model parameters depend on the angular orientation of the template. This angular variation cannot be explained by random measurement error. To quantify the orientation error, measurements are made for 30 different angular rotations of the template for one side of sample #36. The 30 rotation angles are marked on the template at 12° increments ($12 \times k$, where $k = 0, \ldots, 29$). Data were taken at randomly selected angles. A plot of the mean thickness estimates and their associated "one-sigma" error bars (based on eq. (108)) at each angle of rotation is shown in Figure 10. The data indicate that there is no systematic variation of the estimated sample thickness as a function of angle.

The error in $\hat{\bar{b}}$ due to the angular orientation of the template was estimated using a variance components analysis based on the 30 estimates of mean thickness from the polynomial model. The error in angular orientation is assumed to be the same for all samples.

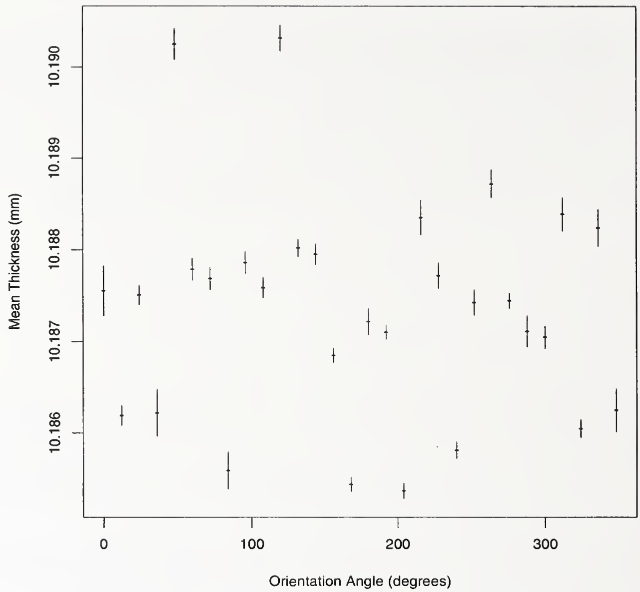

Figure 10. Estimated mean thickness of one side of sample #36 with associated uncertainty intervals ($\pm$ standard error $(\hat{\bar{b}})$, (107)) for 30 different template orientations. The uncertainties were computed based on the assumption that the model (eq. (102)) is valid.

5.2 Environmental Variables

5.2.1 Speed of Light

Determining the speed of light c_{air} in the air-filled portion of the cylindrical cavity is important not only for the calculation of the sample permittivity and loss tangent, but also for the calculation of the cylindrical cavity diameter and length. Due to the presence of water vapor and oxygen in the air, the speed of light is slightly less in air than in vacuum. From measurements of three environmental variables, namely temperature T, barometric pressure P and relative humidity H, we calculate c_{air} [9] as:

$$c_{air} = \frac{c_{vac}}{1 + N_0}, \tag{112}$$

where

$$N_0 = 10^{-6}(2.588P_1 + 41.6E\theta + 2.39E)\theta, \tag{113}$$

with

$$P_1 = P - E, \tag{114}$$

$$E = \frac{H\theta^5}{41.51 \times 10^{9.834\theta - 10}}, \tag{115}$$

and

$$\theta = \frac{300}{273.15 + T}. \tag{116}$$

We measured temperature in units of Celsius, barometric pressure in units of kilopascals, and relative humidity in percent. The computed value of c_{air} is an estimate of the speed of light in the air-filled portion of the cylindrical cavity. Uncertainties in measurements of the environmental variables P, H, and T lead to uncertainty in our estimate of c_{air}.

5.2.2 Temperature

The temperature of the cavity was controlled by a constant-temperature circulating water bath. A thermometer in the water bath in conjunction with a remote thermometer in the water jacket surrounding the cylindrical cavity provide feedback to the temperature controller. After setting the water bath temperature controller to 23 C, we allowed 30 minutes for the cylindrical cavity to reach thermal equilibrium. At that point, the two thermometers are in agreement.

5.2.3 Relative Humidity

We measured the relative humidity with a sling psychrometer that meets a recommendation of the U.S. National Weather Service. It is made up of two mercury-filled thermometers mounted on a stainless steel platform. One bulb has a wick attached that is moistened with deionized water, while the other bulb remains dry. Spinning the two thermometers until the

temperatures reach equilibrium gives the wet-bulb and dry-bulb temperatures. From these two temperatures, we determine the relative humidity from high-altitude (3901 to 6100 feet) relative humidity charts provided by the U.S National Weather Service.

5.2.4 Barometric Pressure

We measured the barometric pressure using a Fortin-type mercurial barometer that is traceable back to the National Institute of Standards and Technology. We corrected for both gravity and the temperature of the barometer mercury [10–12]. First we calculated the temperature-corrected barometric pressure P_t using

$$P_t = P_u + C_t, \tag{117}$$

where

$$C_t = P_u \left[\frac{1 + 0.0000184T}{1 + 0.0001818T} - 1 \right] \tag{118}$$

and P_u is the measured, uncorrected barometric pressure reading. Then, we corrected the barometric pressure for gravity using

$$P = P_t - C_g, \tag{119}$$

where

$$C_g = P_t \left[\frac{980.616}{980.665} \left(1 - 0.0026373 \cos(2L) + 0.0000059 \cos^2(2L) \right) - 1 \right] \tag{120}$$

and L is the latitude in degrees north or south. In the case of our laboratory, the latitude is 40 degrees north.

5.3 Cylindrical Cavity Length and Radius

Direct measurement of the length and radius of the cylindrical cavity is difficult because the bottom endplate is not fixed and the cylindrical waveguide is composed of a helical waveguide. Therefore, we determine the cavity length and radius from observed resonant TE_{01p} modes [13] when the cavity is empty. In section 3.2.2, we derived the measured resonance frequency for the pth TE_{01p} resonant mode as

$$f_a(p) = \frac{c_{air}}{2\pi}\left[\left(\frac{j'_{01}}{a}\right)^2 + \left(\frac{p\pi}{L}\right)^2\right]^{\frac{1}{2}} + \epsilon(p), \tag{121}$$

where p takes on the values 22, 23, and 24. The quantity $f_a(p)$ is estimated from a resonance curve for the pth mode by use of the same algorithm developed for estimating $\hat{Q}$ and $\hat{f}_0$ (Section 5.4). Because the cylindrical-cavity walls and endplates have a finite conductivity, the resonant frequency is shifted slightly downwards. We can correct the resonant frequency due to this skin-depth effect [14] as

$$f_a^*(p) = f_a(p) + \frac{f_a(p)}{2Q}, \tag{122}$$

where Q is the measured quality factor of the pth TE_{01p} resonant mode. In our case, the frequency correction was rather small, a mere 70 kHz correction for a resonant frequency f_a of 10 GHz.

One way to estimate a and L is to linearize the above equation so that it is of the form

$$y(p) = \beta_0 + x(p)\beta_1 + \epsilon^*(p),$$

where

$$\begin{aligned} y(p) &= \left(\frac{2\pi f_a^*(p)}{c_{air}}\right)^2, \\ x(p) &= p^2, \\ \beta_0 &= \left(\frac{j_{01}}{a}\right)^2, \end{aligned}$$

and

$$\beta_1 = \left(\frac{\pi}{L}\right)^2.$$

The method of linear least squares is used to determine $\hat{\beta}_0$ and $\hat{\beta}_1$. By minimizing

$$\sum_p [y(p) - \beta_0 - x(p)\beta_1]^2, \tag{123}$$

we obtain

$$\hat{a} = \frac{j_{01}}{\sqrt{\hat{\beta}_0}} \tag{124}$$

and

$$\hat{L} = \frac{\pi}{\sqrt{\hat{\beta}_1}}. \tag{125}$$

Since $f_a(p)$ is measured with error, squaring the measured value introduces a possible systematic estimation error $(\mathrm{E}(f+\epsilon)^2 = \mathrm{E}(f^2)+\mathrm{E}(\epsilon^2)$, assuming $\mathrm{E}(\epsilon) = 0)$. Hence, this method may not be reliable in general.

More generally reliable estimates of a and L are obtained by mimimizing

$$\sum_p [f_a^*(p) - \hat{f}_a^*(p)]^2 \tag{126}$$

by use of a nonlinear fitting technique, which minimizes a general, unconstrained objective function using the analytic gradient and Hessian of the function. The parameter estimates from a linear least squares fit are used as the starting values in the nonlinear algorithm. We minimize the objective function over many sets of randomly selected initial parameter values to avoid local minima. The random initial conditions are simulated by adding random noise to the least-squares estimates. The standard deviation of the random noise is based on the asymptotic standard errors of $\hat{a}$ and $\hat{L}$ from a least-squares fit. The procedure used to compute asymptotic standard errors (ASEs) is similar to the one used for $\hat{Q}$ and $\hat{f}_o$ [15].

5.4 Resonant Frequency and Quality Factor

We estimate the resonant frequency f_0 of the microwave cavity and the corresponding Q factor using a nonlinear parameter estimation algorithm [15]. At the kth frequency, the observed resonance curve is modeled as

$$T_m(f_k) = \frac{T(f_0)}{1 + Q^2(\frac{f_k}{f_0} - \frac{f_0}{f_k})^2} + BG + \epsilon(f_k), \tag{127}$$

where BG is background and $\epsilon(f_k)$ is additive noise. To estimate the parameters in an optimal way, the frequency-dependent noise in the measurement system must first be characterized. The variance of the additive noise is modeled as

$$\mathrm{VAR}(\epsilon(f_k)) = \sigma^2_{\epsilon(f_k)} = \frac{{\gamma^2}_1}{1 + Q^2(\frac{f_k}{f_0} - \frac{f_0}{f_k})^2} + {\gamma^2}_2. \tag{128}$$

The variance function parameters γ_1 and γ_2 are estimated from the residuals computed from a least-squares fit of the resonance curve model to the observed data. Based on the empirical estimates of the variance function parameters, estimates of Q and f_0 are determined by weighted nonlinear least squares.

Given the parameters that characterize the resonance curve (127), and the variance of the additive noise (128), asymptotic statistical theory [16] predicts the covariance of the parameter estimates. For details regarding the estimation of the parameters and the covariance of the parameter estimates, see Reference [15].

The nonlinear fitting routine used to estimate the model parameters minimizes a general, unconstrained objective function using the analytic gradient and Hessian of the objective function [17]. Some difficulty with convergence was encountered since the function would often converge to a local rather than a global minimum. To prevent this problem, the function was minimized for a large number of randomly generated initial conditions. The final parameter estimates are those that yield the smallest value of the objective function.

5.5 Cylindrical Cavity Conductor Losses

In order to accurately measure the sample loss tangent, we characterized the conductive losses in the walls and endplates of the cylindrical cavity. For the cylindrical-cavity endplates, we measured the surface resistance of the two endplates using the Courtney method [18] at 10 GHz. With the Courtney method, a dielectric sample is sandwiched between two metallic plates and a TE_{01p} resonant mode is excited with a pair of coupling loops. This method is normally used to measure the relative permittivity and loss tangent of the dielectric samples. However, if the relative permittivity and loss tangent of the dielectric resonator are known, we can determine the surface resistance of the metallic endplates that sandwich the dielectric resonator. In our case, we machined an oriented, single-crystal sapphire resonator, placed it between two silver plates, and measured its relative permittivity and loss tangent with the Courtney method. Then, substituting one of the silver endplates with one of the cylindrical-cavity endplates, we measured the surface resistance of the top and bottom cylindrical-cavity endplates at 10 GHz as

$$R_{st} = 39.7 \pm 6.5 \text{ m}\Omega \tag{129}$$

and

$$R_{sb} = 80.7 \pm 5.9 \text{ m}\Omega. \tag{130}$$

The bottom endplate suffers from wear caused by the samples being located directly on the bottom endplate surface, resulting in small scratches. Therefore, we were not surprised to find that the surface resistance of the bottom endplate was significantly higher than that of the top endplate, which has no contact with any samples. We plan to occasionally remeasure the bottom endplate in order to monitor the increase in surface resistance over time. At some point, the surface resistance of this endplate will reach a value where remachining and polishing of the surface will become necessary in order to reduce the metal losses.

Once the surface resistance of the two cylindrical-cavity endplates was measured, we determined the surface resistance of the cavity walls from a measurement of the quality factor for the resonant mode. In section 3.2.3, we found an expression for the quality factor of a TE_{01p} mode:

$$Q = \frac{\frac{c_{air}\mu_0}{2}\left[\left(\frac{j'_{01}}{a}\right)^2 + \left(\frac{p\pi}{L}\right)^2\right]^{3/2}}{\frac{1}{L}\left(\frac{p\pi}{L}\right)^2 [R_{sb} + R_{st}] + \frac{1}{a}\left(\frac{j'_{01}}{a}\right)^2 R_{sw}}. \tag{131}$$

In this expression, R_{st} and R_{sb} represent the surface resistance of the top and bottom endplates respectively, while R_{sw} is the surface resistance of the cavity walls. Solving for R_{sw} we obtain

$$R_{sw} = \frac{\frac{c_{air}\mu_0}{2Q}\left[\left(\frac{j'_{01}}{a}\right)^2 + \left(\frac{p\pi}{L}\right)^2\right]^{3/2} - \frac{1}{L}\left(\frac{p\pi}{L}\right)^2 [R_{sb} + R_{st}]}{\frac{1}{a}\left(\frac{j'_{01}}{a}\right)^2}. \tag{132}$$

Given the measured quality factor Q of the TE_{01p} mode and the measured surface resistance of the two cavity endplates, we can calculate R_{sw} from eq. (132).

6. Permittivity and Loss Tangent Measurements

In this section we outline the step-by-step procedure used to measure the permittivity and loss tangent of the cross-linked polystyrene SRM samples in the NIST 60 mm cylindrical cavity at 10 GHz. We show individual measurements for the 18 samples characterized. In order to verify the cross-linked polystyrene measurements made with the cylindrical cavity, we also show measurements near 10 GHz using four other measurement methods. Although we certify the cross-linked polystyrene properties at 10 GHz, we also made measurements from 8 to 11 GHz in the cylindrical cavity to show how the relative permittivity and loss tangent vary as a function of frequency.

6.1 Measurement Procedure

6.1.1 Speed of Light in Laboratory

An important first step is to determine the speed of light c_{air} in the air-filled portion of the cylindrical cavity, since we need this quantity not only for the calculation of the sample permittivity and loss tangent, but also for the calculation of the length and diameter of the cylindrical cavity. First, we allowed the water bath that circulates water around the cylindrical cavity at 23 °C to reach equilibrium for approximately 30 minutes. Next, we measured the relative humidity with a sling psychrometer. Then we measured the barometric pressure with a Fortin-type mercurial barometer. With these three measured quantities, namely temperature, relative humidity, and barometric pressure, we calculated c_{air} as outlined in Section 5.2.1.

6.1.2 Sample Thickness

The next step in the process was to measure the sample thickness b. We placed a circular template, shown in Figure 9, on top of the sample, and using a Sylvac probe, we measured the thickness of the sample at the 21 template hole locations. In order to calculate the sample thickness, we also measured the diameter of the sample with a dial caliper. Then, using the algorithm outlined in Section 5.1, we calculated the sample thickness.

6.1.3 Cylindrical Cavity Length and Radius

Because the bottom endplate of the cylindrical cavity is not fixed and the cavity walls are composed of helical waveguide, the cavity length L and radius a were difficult to measure directly. In Section 3.2.2, we derived an equation for the resonant frequency f_{01p} of an TE_{01p} mode in an empty cavity:

$$f_{01p} = \frac{c_{air}}{2\pi}\left[\left(\frac{j_{01}}{a}\right)^2 + \left(\frac{p\pi}{L}\right)^2\right]^{\frac{1}{2}}. \tag{133}$$

Note that the resonant frequency depends on both the cavity length and radius, so by measuring several resonant frequencies, we can calculate L and a. First, with the motorized drive below the bottom endplate, we adjusted the length of the empty cavity until the $TE_{01\,23}$ mode resonated at 10 GHz. We then measured the resonant frequencies of the $TE_{01\,22}$, $TE_{01\,23}$, and $TE_{01\,24}$ modes using the method described in Section 5.4. The measured resonant frequency was lowered slightly by the penetration of the electromagnetic fields into the conductive wall and endplates of the cylindrical cavity. To minimize this potential systematic error in L and a, we corrected each of the measured resonant frequencies $f_{m_{01p}}$ [14] using

$$f_{01p} = f_{m_{01p}} + \frac{f_{m_{01p}}}{2Q_{m_{01p}}}, \tag{134}$$

where $Q_{m_{01p}}$ is the measured quality factor of the f_{01p} mode. In the case of the $TE_{01\,23}$ mode, the resonant frequency was approximately 10 GHz with a quality factor near 70 000, so the resonant-frequency correction, due to the skin depth, was under 100 kHz or 0.001 %.

With the three corrected resonant frequencies and eq. (133), we use the method of least squares to determine the cavity length and diameter, as outlined in Section 5.3. With the cavity dimensions determined, we zeroed the digital probe that monitors the travel of the bottom endplate.

6.1.4 Empty Cavity Measurement

Once the cavity dimensions had been calculated, the next step was to characterize the wall and endplate losses of the cylindrical cavity at 10 GHz. This is a very important step as the conductive losses in the cavity are significant and must be properly accounted for in order to accurately measure the loss tangent. The conductive losses vary as a function of frequency, so characterizing these losses at the frequency of interest is also important.

As summarized in Section 5.5, we had previously measured the surface resistances of the top and bottom cavity endplates R_{st} and R_{sb} at 10 GHz using the Courtney method. Therefore, the remaining conductive loss left to characterize was the surface resistance of the cylindrical cavity wall R_{sw}. We measured the resonant frequency and quality factor of the $TE_{01\,23}$ at 10 GHz. From the measured resonant frequency and quality factor, as well as the dimensions of the cylindrical cavity and surface resistances of the two endplates, we can calculate R_{sw} using the method described in Section 5.5.

6.1.5 Sample-Loaded Cavity Measurement

In previous steps, we had already calculated the speed of light, cavity dimensions, and the cavity losses due to the conductive cavity wall and endplates. Left remaining was the measurement of the sample's relative permittivity and loss tangent. We began by lowering the lower endplate assembly, shown in Figure 4. We placed the sample on the bottom

endplate and raised the endplate assembly back into its original position as shown in Figure 3. The presence of the sample inside the cavity shifts the resonant frequency of the $TE_{01\,23}$ mode significantly. Since we characterized the conductive losses at 10 GHz, the cavity must be retuned such that the $TE_{01\,23}$ mode resonates again at 10 GHz for the sample-loaded cavity. Using the motorized drive below the bottom endplate, we retuned the resonant frequency by shortening the cavity by a length ΔL. Since we zeroed the electronic probe monitoring the bottom endplate movement after we measured the cavity length L and radius a, the electronic probe can measure ΔL, the change in the cavity length, directly. Once the $TE_{01\,23}$ mode was tuned to 10 GHz, we measured the resonant frequency and quality factor using the method described in Section 5.4.

At this point, we had completed all the measurements necessary to calculate the sample relative permittivity and loss tangent. First, we calculated the sample's relative permittivity using the transcendental equation we derived in Section 3.3.3:

$$\frac{\tan(\beta_s b)}{\beta_s} + \frac{\tan\left[\beta_0(L-b)\right]}{\beta_0} = 0, \tag{135}$$

where β_s is a function of the sample's relative permittivity ϵ_s'. In order to calculate the relative permittivity from this equation we used the Newton-Raphson iterative method. Since the method is iterative, an initial guess for the relative permittivity was necessary.

Once the sample's relative permittivity was determined, we explicitly calculate the loss tangent using the equation derived in section 3.3.4:

$$\tan\delta_s = \left[\frac{\omega(W_a+W_s)}{Q} - P_{ws} - P_{wa} - P_b - P_t\right]\left\{A_1^2\epsilon_0\epsilon_s'\frac{\pi\omega^3\mu_0^2a^2}{8k^2}J_0^2(ka)\left[2b - \frac{\sin(2\beta_s b)}{\beta_s}\right]\right\}^{-1}. \tag{136}$$

6.2 Relative Permittivity and Loss Tangent Results

In order to verify the long-term stability of our relative permittivity measurements and optimize the measurement procedure, we performed a repeatability study, described in detail in Section 7.2. In this study, we measured three samples: a single-crystal quartz check standard, and two (#9 and #36) cross-linked polystyrene samples (see Figure 7). Once the repeatability study was completed we machined 16 additional cavity samples taken from various parts of the cross-linked polystyrene sheet, as shown in Figure 7. The 16 samples form the first set of SRM samples.

Using the procedure described in the last section, we measured the relative permittivity and loss tangent of all eighteen cross-linked polystyrene samples at 10 GHz using the cylindrical cavity. We collected three sets of data for relative permittivity, shown in Table 1, and loss tangent, shown in Table 2. Each set of eighteen cross-linked polystyrene measurements, as well as two single-crystal quartz check-standard measurements, were collected on a single day, allowing for a week between each set of measurements. As shown in Table 1, the

Table 1. Measured relative permittivity for cross-linked polystyrene SRM samples.

Sample number	Measurement 1	2	3	Average ϵ_s'
9	2.5353	2.5340	2.5351	2.535
10	2.5363	2.5357	2.5345	2.536
12	2.5338	2.5346	2.5341	2.534
15	2.5357	2.5338	2.5334	2.534
16	2.5349	2.5349	2.5324	2.534
17	2.5357	2.5345	2.5341	2.535
24	2.5341	2.5348	2.5329	2.534
28	2.5343	2.5345	2.5332	2.534
29	2.5350	2.5341	2.5343	2.534
36	2.5352	2.5354	2.5359	2.536
37	2.5351	2.5343	2.5347	2.535
41	2.5348	2.5342	2.5368	2.535
48	2.5338	2.5342	2.5356	2.535
49	2.5354	2.5328	2.5338	2.534
50	2.5356	2.5349	2.5353	2.535
53	2.5358	2.5350	2.5333	2.535
55	2.5372	2.5353	2.5343	2.536
56	2.5363	2.5340	2.5333	2.535

range of values for the average relative permittivity varied between 2.534 and 2.536 for all 18 samples while the average loss tangent ranged from 4.6×10^{-4} to 4.7×10^{-4}. This variation in both the relative permittivity and loss tangent is less than or equal to the measurement uncertainty calculated for relative permittivity and loss tangent as shown in Section 7.3. Consequently, within measurement precision, we were not able to detect any variation in the dielectric properties as a function of the sample position on the cross-linked polystyrene sheet, thus verifying our original assumption of the material's homogeneity.

6.3 Measurement Intercomparison

As a consistency check, we compared the relative permittivity and loss tangent data of the cross-linked polystyrene with data from four other measurement methods operating near 10 GHz. These methods included the parallel plate resonator, split-cylinder resonator, dielectric resonator, and another cylindrical cavity [19]. We machined samples for these other methods from the first row of the sheet where the SRM materials were taken. Figures 11 and 12

Table 2. Measured loss tangent for cross-linked polystyrene SRM samples.

Sample number	Measurement 1	2	3	Average $\tan\delta_s(\times 10^4)$
9	4.59	4.60	4.61	4.6
10	4.69	4.66	4.74	4.7
12	4.59	4.59	4.61	4.6
15	4.64	4.61	4.57	4.6
16	4.59	4.60	4.58	4.6
17	4.71	4.68	4.66	4.7
24	4.61	4.61	4.65	4.6
28	4.64	4.65	4.60	4.6
29	4.68	4.61	4.65	4.6
36	4.62	4.62	4.59	4.6
37	4.69	4.68	4.70	4.7
41	4.74	4.67	4.69	4.7
48	4.63	4.62	4.65	4.6
49	4.70	4.65	4.61	4.7
50	4.74	4.71	4.67	4.7
53	4.66	4.63	4.63	4.6
55	4.64	4.57	4.59	4.6
56	4.66	4.66	4.66	4.7

compare the permittivity and loss tangent measurements using the four methods. Also shown in this plot are data for one of the cross-linked polystyrene measurements made with the 60 mm cylindrical cavity. As seen in Figures 11 and 12, there is very good agreement between the 60 mm cylindrical cavity results and measurement made using the four other techniques.

6.4 Broadband Measurements

Although we certified the permittivity and loss tangent of the cross-linked polystyrene material at 10 GHz, we made additional measurements using the cylindrical cavity resonator over a wider frequency range. Using eleven TE_{01n} modes between $n = 16$ and $n = 26$ we were able to cover the frequency range between 8 to 11 GHz. Above 11 GHz, we encountered difficulty in making measurements, due to the presence of interfering, higher-order resonant modes. Although higher-order modes do not propagate below 8 GHz, the quality factors of the TE_{01n} modes are relatively small, thereby decreasing the measurement sensitivity.

Shown in Figures 13 and 14 are the measured permittivity and loss tangent of the cross-linked polystyrene as a function of frequency. Note that the permittivity is relatively flat, which is expected for a low-loss material, while the loss tangent increases with frequency.

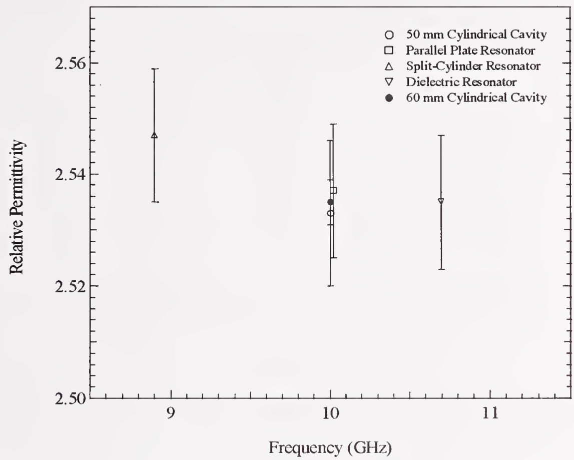

Figure 11. Comparison of cross-linked polystyrene relative permittivity measurements.

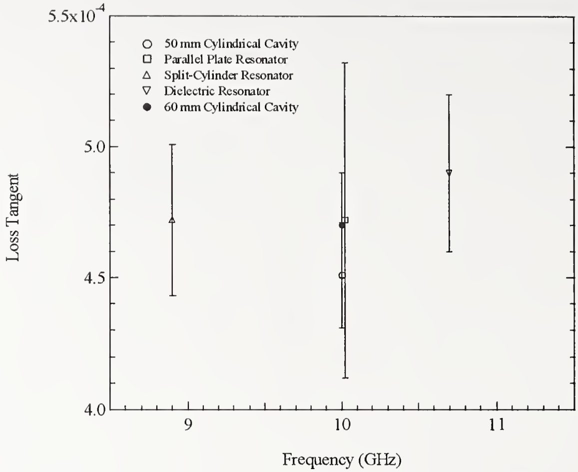

Figure 12. Comparison of cross-linked polystyrene loss tangent measurements.

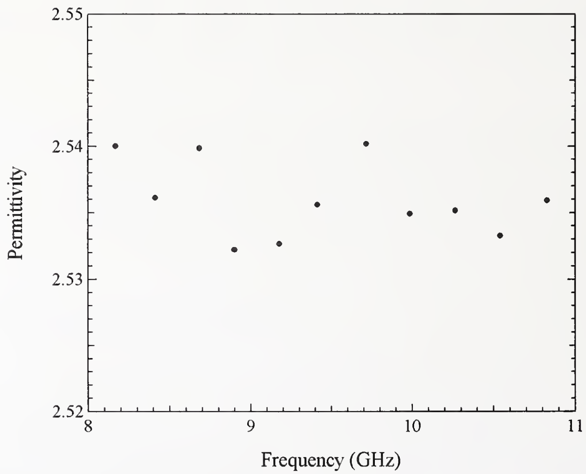

Figure 13. Relative permittivity of cross-linked polystyrene measured in cylindrical cavity resonator.

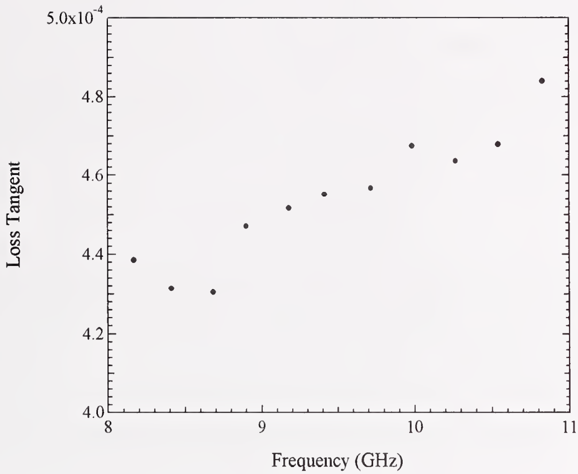

Figure 14. Loss tangent of cross-linked polystyrene measured in cylindrical cavity resonator.

7. Uncertainty Analysis

Estimates of permittivity and loss tangent are uncertain due to both random and systematic errors. In a repeatability study, we quantify uncertainties due to random variability in some, but not all, measured quantities. By a Monte Carlo method, we quantify the effects of two random errors that are not captured in the repeatability study. Using the same Monte Carlo method, the effects of systematic errors on uncertainty are also quantified. Assuming validity of the model, the Monte Carlo approach allows us to estimate the effect of random errors in measured quantities, one at a time or jointly, on the estimates. Based on the repeatability study, we demonstrate the stability of the measurement process. A measurement assurance program based on the repeatability study data is described in Section 8.

7.1 Monte Carlo Simulation Model

The simulation studies utilize a computer program for simulating the effects of random and systematic errors on the measurement process.

7.1.1 Random Errors

Theoretical Study

Based on nominal values and their associated standard deviations for an actual sample (Table 3), we quantify the effect of random errors on estimates of permittivity and loss tangent (Table 4). Standard deviations for T_c, T_B, H, and P_u are based on stated bounds for measurement error provided by the instrument manufacturers. To compute a standard deviation from the upper and lower bounds, we assume that error is a uniformly distributed random variable. Table 4 lists uncertainties in intermediate quantities (c_{air}, a, L) as well as in the permittivity and loss tangent. The individual and joint effects of uncertainties are shown in Table 4.

Based on results in Table 4, the random variability of estimates of c_{air}, a, L, and permittivity is due mostly to random variation in the humidity measurement. However, random errors in estimates of the quality factors Q_a and Q_s are the biggest contributors to uncertainty in the estimate of loss tangent.

The random errors for Q and f_0 correspond to variability expected in a single measurement at a particular time. Repeatability studies reveal additional random variability due to long-term variability in the measurement system. The approximate standard deviations associated with the total (long-term and short-term) random variability are 200 and 400 for Q_a and Q_s, and 11 000 Hz and 14 000 Hz for f_a and f_s. Tables 3 and 4 do not account for long-term measurement variability.

Although the measured values of endplate resistances, $R_{sb,10GHz}$ and $R_{st,10GHz}$, are uncertain, they were not remeasured during the repeatability study; they were measured once and

Table 3. Nominal values of measured and estimated quantities and their standard deviations for cross-linked polystyrene sample #36.

Variable	Nominal Value	Standard Deviation
B_{Lat} (degrees)	39.995	0.00
ΔL (m)	0.0086994	0.00
T_c (°C)	22.9	0.06
T_B (°C)	20.7	0.06
H (%)	44 %	1.2 %
P_u (mm of Hg)	632.1	0.3
$R_{sb,10GHz}$ (Ω/m^2)	0.0807	5.9E-03
$R_{st,10GHz}$ (Ω/m^2)	0.0397	6.5E-03
b (m)	0.01018566	
Measurement		1.5E-07
Template Angular Orientation		1.2E-06
f_s (Hz)	10.00002407E09	145
f_a (Hz)	10.00000897E09	49
Q_s	45223.0	121
Q_a	73945.0	99
$f_a(TE_{0123})$ (Hz)	9.728749568E09	61
$f_a(TE_{0124})$ (Hz)	10.000004096E09	40
$f_a(TE_{0125})$ (Hz)	10.275665920E09	44
$Q(TE_{0123})$	69493.461	125
$Q(TE_{0124})$	73822.742	84
$Q(TE_{0125})$	75711.453	85

treated as constants throughout the study. Similarly, the angular template orientation for the sample thickness measurement was fixed for each sample throughout the repeatability study. Thus, the random errors due to endplate resistance and template angular orientation are not quantified by the repeatability study. The uncertainty associated with these errors was added to the overall uncertainty separately from the random measurement error.

Table 4. Uncertainty of permittivity and loss tangent due to random effects when sources of uncertainty are perturbed individually and jointly (see last line).

Source	Std. Dev.	$U_{c_{air}}$ (m/s)	U_a (m)	U_L (m)	$U_{\epsilon'_s}$	$U_{\tan\delta_s}$
T_c	0.06 °C	36.2	3.63E-09	5.25E-08	1.06E-06	6.25E-11
T_B	0.06 °C	0.6	6.33E-11	9.17E-10	1.85E-08	1.09E-12
H	1.2 %	411.6	4.12E-08	5.97E-07	1.20E-05	7.10E-10
P_u	0.3 mm of Hg	30.3	3.03E-09	4.39E-08	8.85E-07	5.22E-11
$R_{sb,10GHz}$	5.9E-03 Ω/m^2					4.67E-07
$R_{st,10GHz}$	6.5E-03 Ω/m^2					5.13E-07
b Measurement	1.5E-07 m				1.30E-10	7.11E-11
b Angular	1.2E-06 m				1.13E-09	5.76E-10
f_s	144.6 Hz				4.22E-06	5.93E-10
f_a	48.9 Hz					1.17E-12
Q_s	121.5					3.31E-06
Q_a	99.4					1.05E-06
$f_a(p)$	60.5, 39.9, 43.9 Hz		3.56E-09	2.97E-08	8.32E-07	1.23E-10
$Q(p)$	124.9, 83.8, 85.0		7.06E-09	5.87E-08	1.49E-06	2.29E-10
All		412.7	4.18E-08	6.05E-07	1.29E-05	3.52E-06

7.1.2 Systematic Errors

Cavity Radius a and Length L

We studied the systematic error associated with the position of the cavity endplate for the estimates of a and L. Thirty pairs of (a, L) measurements were taken at 30 different elevations of the cavity endplate (Figure 15). Holding all other parameters and measured quantities fixed to values used in Table 3, permittivity and loss tangent were estimated for perturbed values of a and L (from the Table 3 measurement) based on the deviations of the 30 (a, L) pairs from their associated mean values. We also estimated loss tangent and permittivity for each of the 30 deviations of a or L individually (the other parameter was equated to its mean value.) To quantify systematic error due to uncertainty in a and L, the standard deviations of the 30 estimates of permittivity and loss tangent (Table 5) were computed. Parenthetically, the propagation-of-errors approximation for the standard deviation of the estimates of permittivity or loss tangent is very poor unless the covariance structure is accounted for.

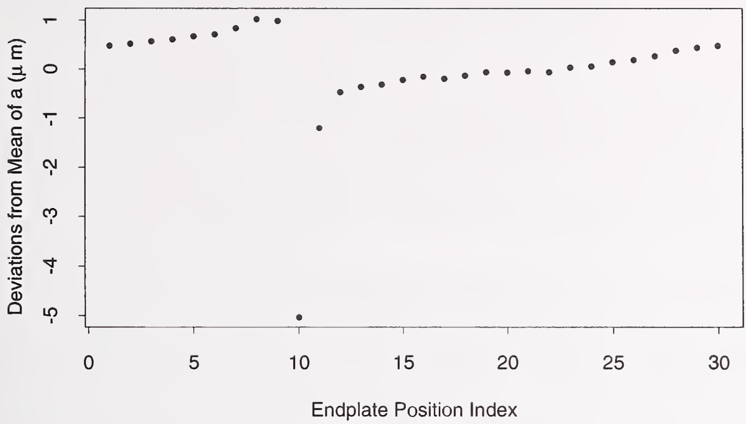

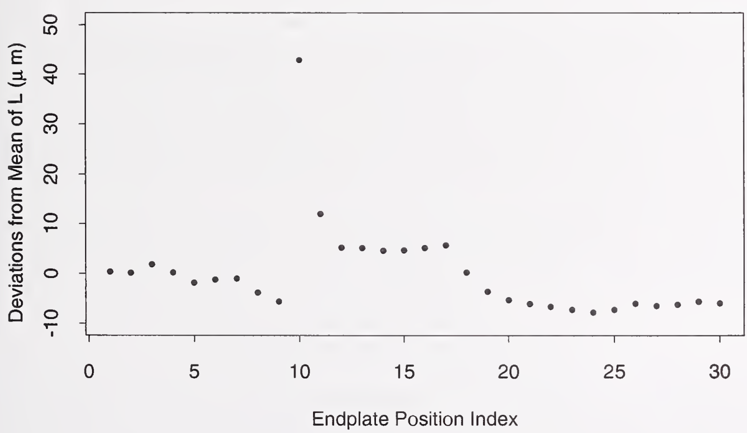

Figure 15. $\hat{a} - \overline{\hat{a}}$ versus endplate position index (top), and $\hat{L} - \overline{\hat{L}}$ versus endplate position index (bottom).

Table 5. Uncertainties of ϵ_s' and $\tan\delta_s$ due to systematic errors in a and L.

Type of Estimate	$U_{\epsilon_s'}$	$U_{\tan\delta_s}$
Monte Carlo Simulation		
Vary a	3.7E-03	5.4E-07
Vary L	4.1E-03	5.5E-07
Vary a and L	1.9E-03	2.7E-07
Propagation of Errors		
Without Covariance	5.5E-03	7.7E-07
With Covariance	1.9E-03	2.7E-07

Sample Thickness, b

We studied the uncertainty in permittivity and loss tangent due to systematic errors in sample thickness b using the simulation model. The two sources of systematic error are inexact knowledge of both the sample radius and the probe error.

For each source of error, the appropriate standard deviation was used to perturb the value of b in the simulation model while all other parameter values were held constant. The standard deviation of the resulting permittivity and loss tangent represents the uncertainty for the source of error being quantified.

The value of standard deviation (s_B) used in the simulation model for estimating the uncertainty of permittivity and loss tangent due to the sample radius was based on the worst-case (or maximum) error observed in the template angular orientation study. (See Section 5.1 for details regarding estimation of sample thickness.) Although s_B is dependent in part on the estimated model parameters (see eq.(109)), s_B is considered systematic because the sample radius was measured on one occasion and was constant for all subsequent measurements of permittivity and loss tangent.

Probe error is the manufacturer's specified error for measurements of sample thickness provided by the probe. The simulation model utilizes a standard error of b based on a uniform distribution bounded by the manufacturer's specifications (see section 7.1.1).

Change in Cavity Length ΔL

We determined the uncertainty in estimates of permittivity and loss tangent due to systematic errors in ΔL using the simulation model. (See Section 6.1.5 for details regarding ΔL.) Systematic errors in ΔL are caused by inexact knowledge of the distance traveled by the cavity endplate after the sample is loaded. The standard error of ΔL was based on a uniform distribution bounded by the manufacturer's specifications of the probe accuracy.

Frequency Drift

In the measurement process, a resonance curve T was sampled at 201 frequencies. The kth frequency is

$$f_k = f_{ref} + (k - 101)df, \tag{137}$$

where $f_{ref} = 10$ GHz and df is the frequency spacing. For each frequency f_k, we simulated 500 values of T. Over the course of these 500 measurements, we assumed that the resonance frequency was drifting upward in a linear fashion. For each f_k, we averaged the 500 simulated values of T. At the first measurement of $T(f_1)$, $f_0 = f_{ref}$. During the last measurement of $T(f_{201})$, $f_0 = f_{ref} + \delta$, where δ is frequency drift. Finally, the simulated resonance curve was normalized so that its maximum value is 1.

A four-parameter model (with flat background) was fitted to the noise-free simulated resonance curve using the method of least squares. The difference between $\hat{Q}$ and Q is the estimated bias in $\hat{Q}$. The bias of the resonance frequency estimator, $\hat{f_0}$ was estimated in a similar manner. Figure 16 displays the bias of $\hat{Q}$ and $\hat{f_0}$ versus frequency spacing df for $Q = 50\ 000$ and four levels of resonance frequency drift.

The bias of $\hat{Q}$ was approximated as follows:

$$-\mathrm{BIAS}(\hat{Q}) \approx \left(\frac{df}{f_{ref}}\right)^{\alpha_1} \left(\frac{\delta}{f_{ref}}\right)^{\alpha_2} \times\ 10^{\alpha_3}, \tag{138}$$

where $f_{ref} = 1$ GHz, $\hat{\alpha_1} = -1.000004$, $\hat{\alpha_2} = 396455.6$, and $\hat{\alpha_3} = -4.05579$ when $Q = 50\ 000$.

We estimated the bias of $\hat{Q}$, for a specific frequency drift using (138). Based on repeated observations of resonance curves, the frequency drift was estimated to be at most 500 Hz.

For frequency spacings of 3500 Hz (empty cavity) and 5600 Hz (sample-loaded cavity), 1000 random values of drift between zero and 500 Hz were simulated. For each realization of the frequency drift, we estimated the bias in the Q estimate using eq. (138), and estimated both permittivity and loss tangent (holding all other variables fixed). We quantified the uncertainty in the estimates of permittivity and loss tangent due to frequency drift by computing the standard errors of these 1000 estimates of permittivity and loss tangent.

7.2 Observational Repeatability Study

We quantified both short-term and long-term variation to determine the stability of the measurement process. In general, a repeatability study captures much more variability than does a theoretical study because actual measurements typically depend on sources of variability not accounted for in theoretical simulation models. Based on the repeatability study data, we determine the statistical significance of the effects of four factors (sample orientation, operator, sample number, and measurement day) on the measured values of permittivity and loss tangent.

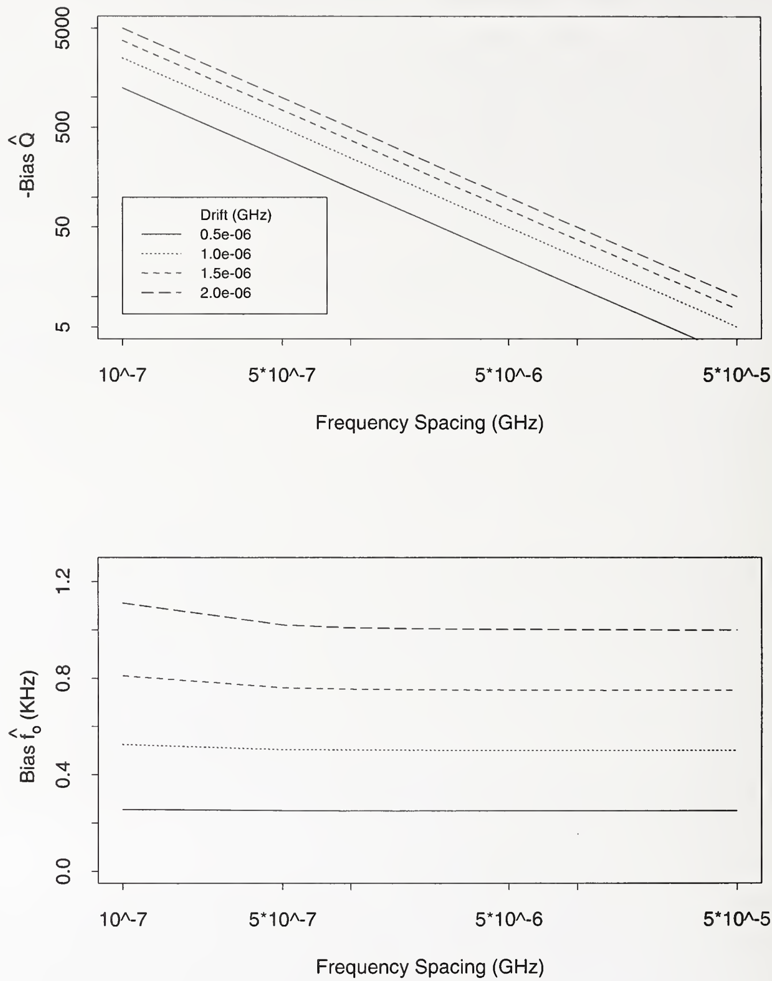

Figure 16. Estimated bias of $\hat{Q}$ and $\hat{f}_0$ for $Q = 50\ 000$.

The measurement plan requires two operators to measure each of two cross-linked polystyrene samples (#9 and #36) for two orientations (up and down) on eight different occasions. The template specifying coordinates for sample thickness measurements is placed in a fixed location on each sample for all thickness measurements. A sample made of single quartz crystal served as a "check standard" and is measured at the beginning of each operator's measurement session. The measurement sequence for the first day of the study is shown in Table 6.

Table 6. Measurement plan for the first day.

Operator number	Sample	Sample orientation
1	Quartz	Down
	#9	Down
	#36	Up
	#9	Up
	#36	Down
2	Quartz	Up
	#36	Down
	#9	Up
	#9	Down
	#36	Up

Measured values of permittivity and loss tangent on the cross-linked polystyrene samples over time are displayed in Figure 17. Figure 18 shows measurements of the single quartz crystal over time. Since Figures 17 and 18 indicate that there are no time trends in the data, we conclude that the measurement process is stable over the duration of the study.

An analysis of variance [20] was performed using the repeat measurement data to: (1) determine whether estimated permittivity and loss tangent are statistically different depending on the orientation of the sample in the cavity; (2) determine whether differences in permittivity and loss tangent among samples are statistically significant; and (3) estimate the contributions of operators and measurement time to the overall variance of the estimates. (See Reference [21] regarding experiment design and analysis.) The four factors and their respective levels used in the analysis of variance are displayed in Table 7.

Table 7. Analysis of variance factors.

Factor name	Symbol	Factor levels
Sample orientation	T_i	Up, Down
Operator	O_j	1,2
Sample Number	S_k	#9, #36
Day	D_l	1, ..., 8

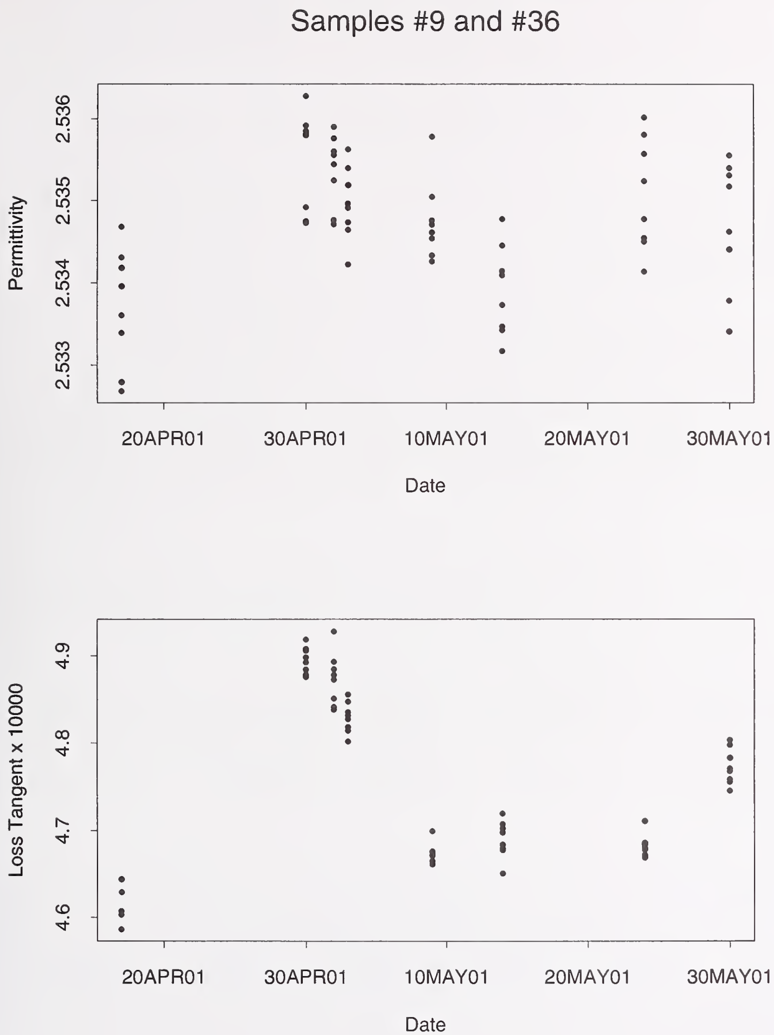

Figure 17. Permittivity and loss tangent of cross-linked polystyrene samples over time.

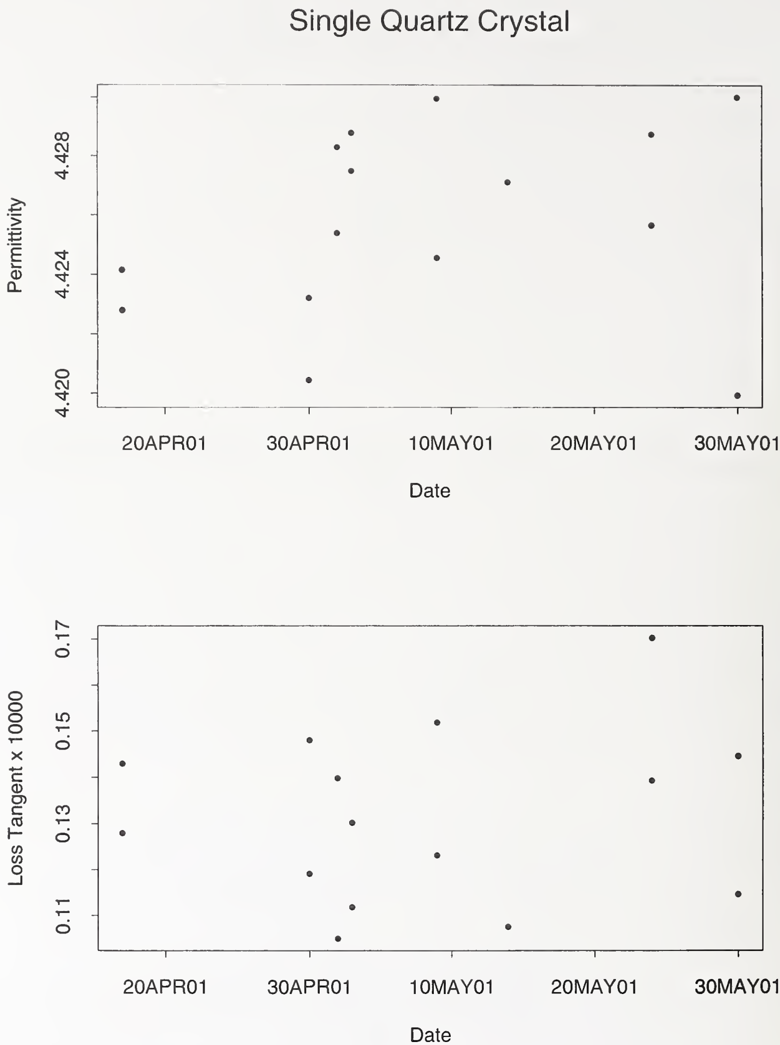

Figure 18. Permittivity and loss tangent of single quartz crystal over time.

The analysis of variance for the cross-linked polystyrene samples is based on the model

$$\begin{aligned} y_{ijklm} &= \mu + T_i + O_j + S_k + D_l + \\ & (TO)_{ij} + (TS)_{ik} + (TD)_{il} + \\ & (OS)_{jk} + (OD)_{jl} + \\ & (SD)_{kl} + \epsilon_{ijklm} \end{aligned} \tag{139}$$

for a single measurement y_{ijklm}, where μ represents the overall mean and ϵ_{ijklm} is a random error component. The terms containing symbols for two factors, such as $(TO)_{ij}$, represent interactions (or dependencies) among the factors. Although the model could include interactions comprised of more than two factors, the general model selected for the analysis is adequate for identifying possible dependencies among the factors.

The analysis of variance reveals that only one factor, measurement day, is significant at the 0.1 level for both permittivity (p-value = 0.10) and loss tangent (p-value = 0.06). Since measurement day is the only significant factor, the total random measurement variation is the sum of the component of variance due to measurement day (called between-day or long-term variation) and the component of variance due to random error (called within-day or short-term variation). Table 8 displays the variance component estimates for permittivity and loss tangent.

Table 8. Estimated variance components for permittivity and loss tangent. The number in parentheses represents the percentage of total variance.

	$\epsilon_s^{'}$		$\tan\delta_s$	
Source	Variance	Stan. dev.	Variance	Stan. dev.
Between-Day	0.41E-06 (51 %)	6.4E-04	0.011E-08 (97 %)	1.04E-05
Within-Day	0.40E-06 (49 %)	6.3E-04	0.037E-10 (3 %)	0.19E-05
Total	0.81E-06	9.0E-04	0.011E-08	1.06E-05

The estimated standard deviation of a single future measurement is the total standard deviation listed in Table 8. This repeat measurement error is one component of the overall uncertainty. The individual components of variance shown in Table 8 can also be used to develop uncertainties for averages of measurements. The percent errors, based on the repeat measurement error divided by the average of all 64 measurements, are 0.035 % for permittivity and 2.2 % for loss tangent.

We also performed an analysis of variance for the single quartz crystal. No factors are statistically significant. The repeat measurement error for permittivity and loss tangent are 0.0033 (0.075 %) and 2.0E-06 (14.7 %), respectively.

After completing the analysis of the repeatability study data, additional measurements were taken for three samples to verify the stability of the measurement system. Plots of the old and new observations reveal a shift in permittivity for the quartz sample (Figure 19). Further investigation suggests that the mean level shift in the quartz data could be related to backlash error in the motorized micrometer. Additional data were collected for the three samples after altering the measurement procedure to minimize backlash error. The new data indicate that the measurement system is now stable. Interestingly, the measurements of cross-linked polystyrene samples do not appear to be effected by the backlash error (Figure 19).

The next step in the analysis is to determine whether the new data can be combined with the old data to produce a better estimate of the repeat measurement error. A mixed-model analysis of variance reveals that the mean levels corresponding to old and new permittivity and loss tangent data associated with cross-linked polystyrene samples are not statistically different. In addition, there is insufficient evidence to suggest that the short-term and long-term variation of the estimates has changed. Thus, we conclude that the old and new cross-linked polystyrene data can be combined. However, the mixed model analysis for the quartz data indicated that the old and new data should not be combined. The repeat measurement errors based on the combined data for cross-linked polystyrene are shown in Table 9.

Table 9. Estimated variance components for permittivity and loss tangent based on combined data. The numbers in parentheses represents the percentage of total variance.

	$\epsilon_s^{'}$		$\tan\delta_s$	
Source	Variance	Stan. dev.	Variance	Stan. dev.
Between-Day	0.40E-06 (49 %)	6.3E-04	0.0086E-08 (96 %)	9.3E-06
Within-Day	0.41E-06 (51 %)	6.4E-04	0.0032E-09 (4 %)	1.8E-06
Total	0.82E-06	9.0E-04	0.0089E-08	9.4E-06

7.3 Relative Permittivity and Loss Tangent Uncertainty

We list all sources of error studied and their effects on the uncertainty of the permittivity and loss tangent estimates in Table 10. The table displays the combined standard uncertainty, which is the square root of the sum of the individual squared uncertainties.

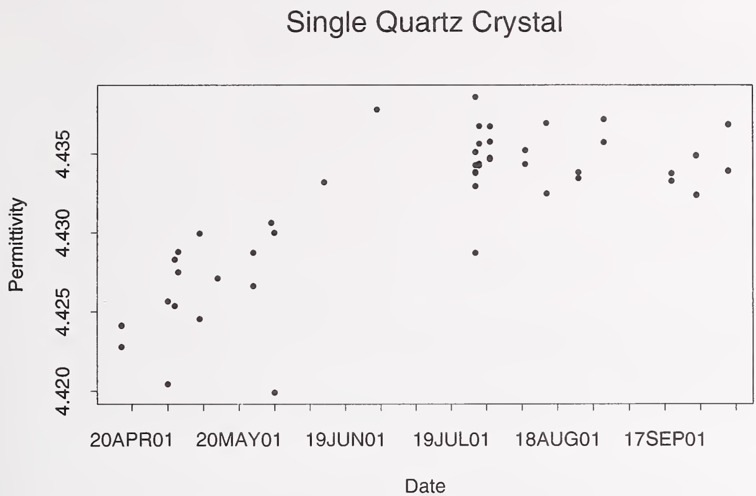

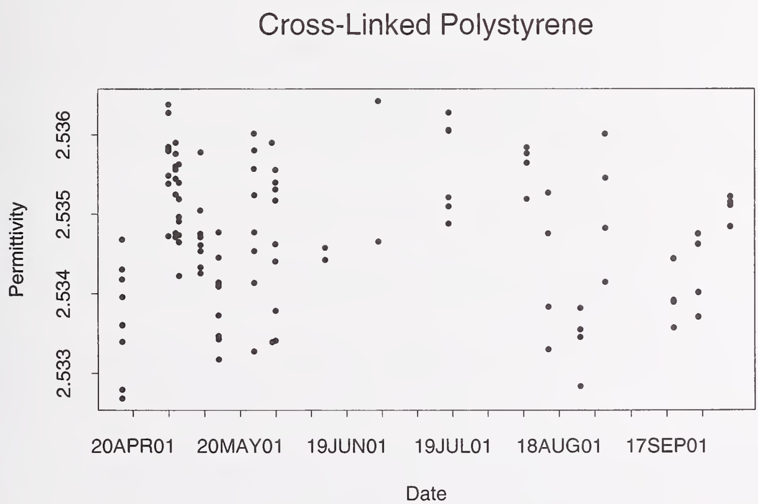

Figure 19. Permittivity single quartz crystal and cross-linked polystyrene over time.

Table 10. Combined standard uncertainty for ϵ_s' and $\tan\delta_s$.

Source of uncertainty	Type of effect	$U_{\epsilon_s'}$	$U_{\tan\delta_s}$
Measurement	Random (A)	9.0E-04	9.4E-06
$R_{sb,10GHz}$	Random (B)		4.7E-07
$R_{st,10GHz}$	Random (B)		5.1E-07
b Template angular orientation	Random (B)	1.1E-09	5.7E-10
b Probe	Systematic (B)	7.7E-10	4.1E-10
Sample radius	Systematic (B)	1.6E-12	9.0E-13
Q Bias due to frequency drift	Systematic (B)	1.1E-07	3.0E-08
a and L	Systematic (B)	1.9E-03	2.7E-07
ΔL Probe	Systematic (B)	3.7E-04	5.2E-08
Combined standard uncertainty, U_C		2.1E-03	9.4E-06
Coverage factor, k		2	2
Expanded uncertainty, kU_C		4.4E-03	1.9E-05

The overall uncertainty for a single measurement (made on any sample, by any operator, and any sample orientation) is the combined standard uncertainty, U_C. The uncertainty due to systematic effects on $\tan\delta_s$ is negligible compared to the combined standard uncertainty.

The certified value that we shall report for each SRM sample is based on three repeated measurements taken over a span of several weeks. Thus, the uncertainties for certified values are slightly different from those reported in Table 10.

To determine the uncertainty for a certified value, we assume that the observed data for the i^{th} sample can be modeled by

$$y_{ijk} = \mu_i + D_j + \epsilon_{ijk} + e_{bprobe} + e_{radius} + e_{Qbias} + e_{aL} + e_{\Delta Lprobe}, \tag{140}$$

where D_j is the j^{th} measurement day, and e_{ijk} is the error of the k^{th} measurement on the j^{th} day (here $k = 1$). The quantities e_{bprobe}, e_{radius}, e_{Qbias}, e_{aL}, and $e_{\Delta Lprobe}$ represent the systematic errors listed in Table 10.

The best estimate of the certified value for a single sample is the simple average of the three measurements. We assume that the correction factors for the systematic errors are zero. However, the correction factors are not known perfectly, and thus have some uncertainty associated with the correction factors.

The combined standard uncertainty associated with the certified value is

$$U_C = \sqrt{(u_D^2 + u_\epsilon^2)/m + u_{bprobe}^2 + u_{radius}^2 + u_{Qbias}^2 + u_{aL}^2 + u_{\Delta Lprobe}^2}, \tag{141}$$

where $m = 3$ (the number of measurement days), u_D and u_ϵ represent the long-term and short-term components of variance (see Table 9 for example), and u_{bprobe}, u_{radius}, u_{Qbias}, u_{aL},

and $u_{\Delta Lprobe}$ represent uncertainties associated with systematic errors. The effective degrees of freedom were computed by use of the Satterthwaite approximation.

8. Measurement Quality Assurance

To ensure the integrity of the measurement system, measurements are performed periodically on three check standards: cross-linked polystyrene samples #9 and #36 and a single quartz crystal sample. New measurements are compared to past measurements using control charts for individual measurements and moving ranges. (The moving range chart contains the differences between adjacent values over time.) The "individuals" control chart monitors the nominal value of the measurements, while the moving range chart is a tool for detecting changes in the variation of the measured values; see Reference [22] for details regarding the construction of control charts.

Examples of control charts for permittivity measurements of cross-linked polystyrene sample #9 are shown in Figure 20. Repeat measurement error and the associated degrees of freedom (determined by the Satterthwaite approximation) from the repeatability study (see Section 7.2) were used to define boundaries for acceptable measurements. The top graph displays a 99.6 % (three-sigma) control chart for single future measurements of $\epsilon_s^{'}$, and the bottom chart is the associated moving range chart.

In addition to traditional control charts, we generated a control *region* for new measurements of the two cross-linked polystyrene check standards completed on the same day. Same-day measurements are related since they will share similar environmental conditions. An elliptical region that contains 99.6% (roughly a $\pm$ three sigma interval) of the bivariate distribution of the two sample measurements, y_1 and y_2, is defined by

$$\frac{(y_1-\mu)^2(\sigma_D^2+\sigma^2) - 2(y_1-\mu)(y_2-\mu)\sigma_D^2 + (y_2-\mu)^2(\sigma_D^2+\sigma^2)}{\sigma^4+2\sigma_D^2\sigma^2} \leq \chi^2_{0.996,2},$$

where μ is the mean permittivity (assumed to be the same for both samples), and σ_D^2 and σ^2 are the between-day and within-day variances, respectively [23]. In the equation, μ, σ_D^2 and σ^2 denote true, but unknown, parameters. The parameters were estimated using the repeat measurement data (see Table 9, Section 7.2, so that the resulting control region is approximate.) Figure 21 displays an approximate 99.6 % elliptical control region for a single pair of future measurements of samples #9 and #36 taken on the same day. The region was generated using $\hat{\mu} = 2.53$, $\hat{\sigma}_D^2 = 0.401\text{E-}06$, and $\hat{\sigma}^2 = 0.414\text{E-}06$.

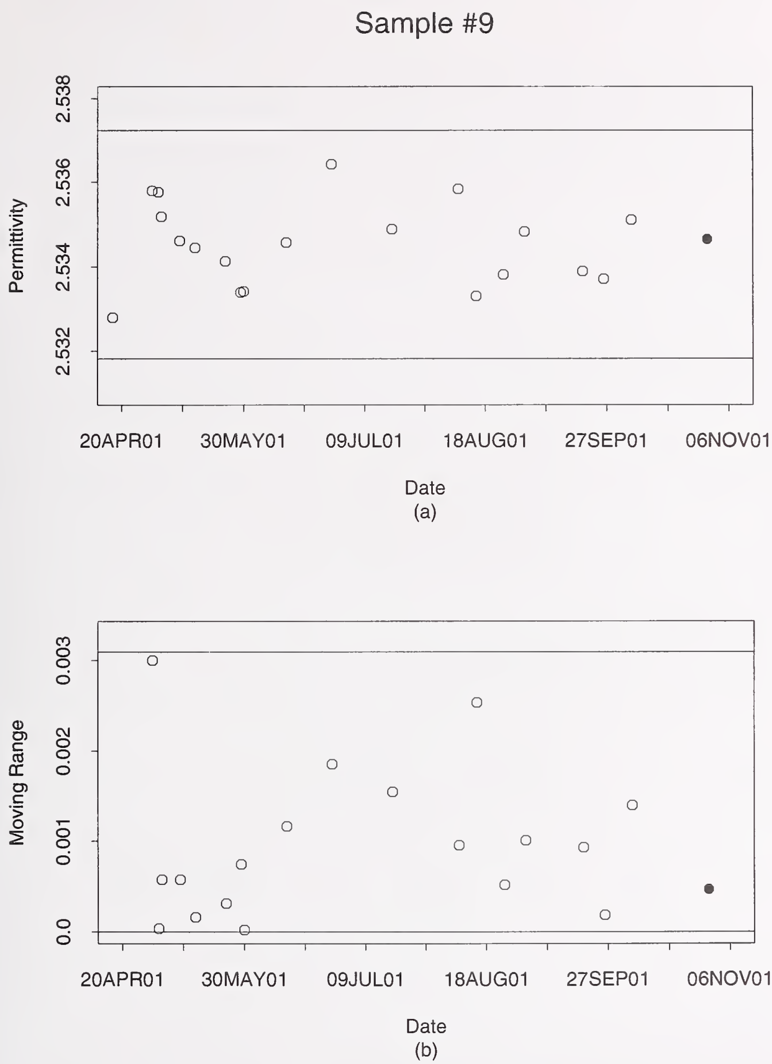

Figure 20. (a) Control chart with 99.6 % probability limits for individual measurements of ϵ_s' for sample #9. (b) Moving range control chart. Circles represent historical data used to generate control limits, while the dot represents a new observation.

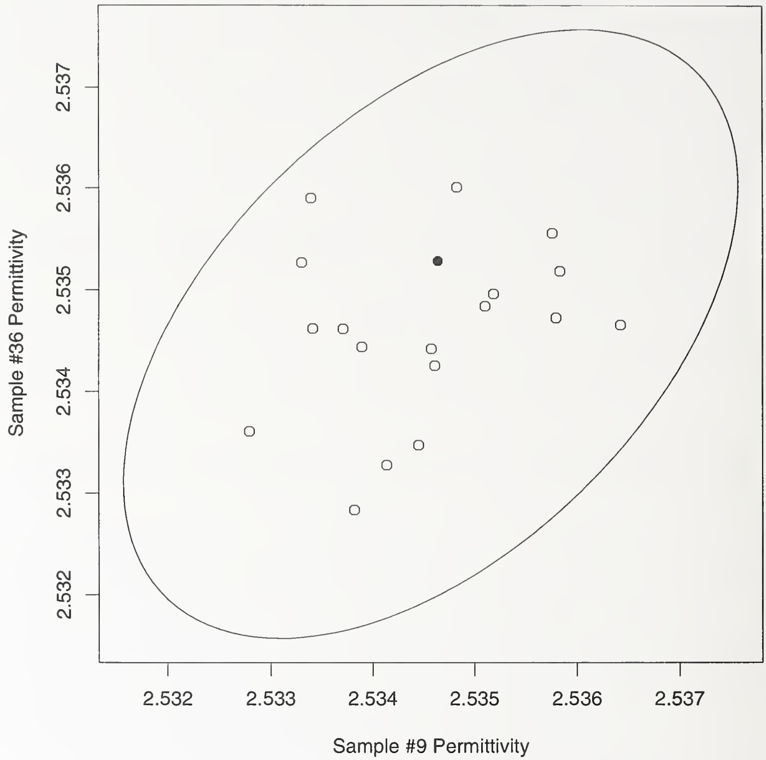

Figure 21. Approximate 99.6 % (three-sigma) bivariate control region for pairs of ϵ_s' measurements. Circles represent historical data, while the dot represents a new observation.

9. Conclusion

We have demonstrated that the circular-cylindrical cavity method has the necessary measurement accuracy to characterize dielectric standard reference materials. Using this method, we were able to measure the relative permittivity of cross-linked polystyrene samples with less than 0.5 percent uncertainty, while the loss tangent uncertainty was less than 2×10^{-5}. This low level of uncertainty was achieved because we identified and characterized many different aspects of the measurement method. Highlights include a new method for measuring a cavity's resonant frequency and quality factor, the inclusion of the surface resistance of the circular-cylindrical cavity's wall and endplates in the measurement theory, and a study of the effects of coupling losses.

In our uncertainty analysis for both the relative permittivity and loss tangent, we identified and characterized the random sources of uncertainty through a comprehensive repeatability study, and also included the effects of several systematic sources of error. To verify the performance of this method, we compared the relative permittivity and loss tangent, measured with the circular-cylindrical cavity, to measurement made in several other resonant techniques and found good agreement. Finally, to ensure the integrity of the measurement system over time, a measurement assurance plan is outlined.

Acknowledgments

The authors acknowledge Dom Vecchia and Hari Iyer for many helpful discussions, and in particular for the development of the uncertainty of the certified value of SRMS. Thanks also to Jack Wang for providing information regarding bivariate control ellipses.

10. References

[1] F. Horner, T.A. Taylor, R. Dunsmuir, J. Lamb, and W. Jackson, "Resonance methods of dielectric measurement at centimetre wavelengths," *Journal of the I.E.E.*, vol. 93, Part III, pp. 53–68, 1946.

[2] R.J. Cook, "Microwave cavity methods," in *High Frequency Dielectric Measurement*, J. Chamberlain and G.W. Chantry, Eds., pp. 12–27. IPC Science and Technology Press, 1973.

[3] E. Ni and U. Stumper, "Permittivity measurements using a frequency-tuned microwave TE_{01} cavity resonator," *IEE Proceedings*, vol. 132, no. 1, pp. 27–32, February 1985.

[4] E. Vanzura, R. Geyer, and M. Janezic, *The NIST 60-Millimeter Diameter Cylindrical Cavity Resonator: Performance for Permittivity Measurements*, Natl. Inst. Stand. Technol. Tech. Note 1354, 1993.

[5] R. Geyer, *Dielectric Characterization and Reference Materials*, Natl. Inst. Stand. Technol. Tech. Note 1338, 1990.

[6] E. Hotston, "Correction term for dielectric measurements with cavity resonators," *J. Sci. Instrum.*, vol. 38, pp. 130–131, April 1961.

[7] V. Poyarkova G. Burdun, E. Zaltsman and V. Frumkin, "Methods for raising precision in measuring the characteristics of dielectrics at ultrahigh frequencies," *Meas. Tech.*, vol. 12, no. 5, pp. 682–687, 1969.

[8] E.B. Zaltsman, "Permittivity measurement error due to a residual gap," *Meas. Tech.*, vol. 11, no. 11, pp. 1516–1519, November 1968.

[9] H. Liebe, "An updated model for millimeter wave propagation in moist air," *Radio Sci.*, vol. 20, no. 5, pp. 1069–1089, September-October 1985.

[10] S. Letestu, *International Meteorological Tables*, World Meteorological Organization, WMO-No. 118TP.94, Geneva, Switzerland, 1966; with amendments thru July 1973.

[11] R. List, *Smithsonian Meteorological Tables*, vol. 114, Smithsonian Miscellaneous Collections, Publication 4014, Smithsonian Institution Press, 6th revised edition 1949, 5th reprint 1971.

[12] *Manual of Barometry*, vol. I, U.S. Department of Commerce, Weather Bureau, Washington D.C., 1963.

[13] J.C. Gallop and W. Radcliffe, "Shape and dimensional measurement using microwaves," *J. Phys. E: Sci. Instrum.*, vol. 19, pp. 413–417, 1986.

[14] R.A. Waldron, *Theory of Guided Electromagnetic Waves*, New York : Van Nostrand Reinhold, 1970.

[15] K. Coakley, J. Splett, M. Janezic, and R. Kaiser, "Estimation of q-factors and resonant frequencies," *IEEE Trans. Microwave Theory Tech.*, vol. 51, no. 3, pp. 862–868, 2002.

[16] Y. Bard, *Nonlinear Parameter Estimation*, Academic Press, 1974.

[17] D. M. Gay, "Computing optimal locally constrained steps," *SIAM Journal on Scientific and Statistical Computing*, vol. 2, pp. 186–197, 1981.

[18] W.E. Courtney, "Analysis and evaluation of a method of measuring the complex permittivity and permeability of microwave insulators," *IEEE Trans. Microwave Theory Tech.*, vol. 18, no. 8, August 1970.

[19] J. Baker-Jarvis, R. Geyer, J. Grosvenor, M. Janezic, C. Jones, B. Riddle, C. Weil, and J. Krupka, "Dielectric characterization of low-loss materials in the range 1 GHz to 20 GHz: A comparison of techniques," *IEEE Trans. Dielect. Elect. Insulation*, vol. 5, no. 4, pp. 571–577, 1998.

[20] G. A. Milliken and D. E. Johnson, *Analysis of Messy Data: Volume 1*, Lifetime Learning Publications, 1984.

[21] G. E. P. Box, W. G. Hunter, and J. S. Hunter, *Statistics for Experimenters*, John Wiley & Sons, 1978.

[22] ANSI/ASQC A1-1987, *Definitions, Symbols, Formulas, and Tables for Control Charts*, American Society for Quality Control, 1987.

[23] F. A. Graybill, *Theory and Application of the Linear Model*, Wadsworth Publishing Co., 1976.

GPO U.S. GOVERNMENT PRINTING OFFICE 2005–773–018/40253

NIST *Technical Publications*

Periodical

Journal of Research of the National Institute of Standards and Technology—Reports NIST research and development in metrology and related fields of physical science, engineering, applied mathematics, statistics, biotechnology, and information technology. Papers cover a broad range of subjects, with major emphasis on measurement methodology and the basic technology underlying standardization. Also included from time to time are survey articles on topics closely related to the Institute's technical and scientific programs. Issued six times a year.

Nonperiodicals

Monographs—Major contributions to the technical literature on various subjects related to the Institute's scientific and technical activities.
Handbooks—Recommended codes of engineering and industrial practice (including safety codes) devel- oped in cooperation with interested industries, professional organizations, and regulatory bodies.
Special Publications—Include proceedings of conferences sponsored by NIST, NIST annual reports, and other special publications appropriate to this grouping such as wall charts, pocket cards, and bibliographies.
National Standard Reference Data Series—Provides quantitative data on the physical and chemical properties of materials, compiled from the world's literature and critically evaluated. Developed under a worldwide program coordinated by NIST under the authority of the National Standard Data Act (Public Law 90-396). NOTE: The Journal of Physical and Chemical Reference Data (JPCRD) is published bimonthly for NIST by the American Institute of Physics (AIP). Subscription orders and renewals are available from AIP, P.O. Box 503284, St. Louis, MO 63150-3284.
Building Science Series—Disseminates technical information developed at the Institute on building materials, components, systems, and whole structures. The series presents research results, test methods, and performance criteria related to the structural and environmental functions and the durability and safety characteristics of building elements and systems.
Technical Notes—Studies or reports which are complete in themselves but restrictive in their treatment of a subject. Analogous to monographs but not so comprehensive in scope or definitive in treatment of the subject area. Often serve as a vehicle for final reports of work performed at NIST under the sponsorship of other government agencies.
Voluntary Product Standards—Developed under procedures published by the Department of Commerce in Part 10, Title 15, of the Code of Federal Regulations. The standards establish nationally recognized requirements for products, and provide all concerned interests with a basis for common understanding of the characteristics of the products. NIST administers this program in support of the efforts of private-sector standardizing organizations.

Order the following NIST publications—FIPS and NISTIRs—from the National Technical Information Service, Springfield, VA 22161.

Federal Information Processing Standards Publications (FIPS PUB)—Publications in this series collectively constitute the Federal Information Processing Standards Register. The Register serves as the official source of information in the Federal Government regarding standards issued by NIST pursuant to the Federal Property and Administrative Services Act of 1949 as amended, Public Law 89-306 (79 Stat. 1127), and as implemented by Executive Order 11717 (38 FR 12315, dated May 11,1973) and Part 6 of Title 15 CFR (Code of Federal Regulations).
NIST Interagency or Internal Reports (NISTIR)—The series includes interim or final reports on work performed by NIST for outside sponsors (both government and nongovernment). In general, initial distribution is handled by the sponsor; public distribution is handled by sales through the National Technical Information Service, Springfield, VA 22161, in hard copy, electronic media, or microfiche form. NISTIR's may also report results of NIST projects of transitory or limited interest, including those that will be published subsequently in more comprehensive form.

U.S. Department of Commerce
National Bureau of Standards and Technology
325 Broadway
Boulder, CO 80305-3328

Official Business
Penalty for Private Use $300